Nuclear Physics B69 (1974) 454–492. North-Holland Publishing Company

MULTIPLICITIES, TOPOLOGICAL CROSS SECTIONS, AND SINGLE PARTICLE INCLUSIVE DISTRIBUTIONS FROM pp INTERACTIONS AT 12 AND 24 GeV/c

V. BLOBEL*, G.W. BRANDENBURG[×±], H. FESEFELDT*, H. FRANZ[×], B. HELLWIG*, U. IDSCHOK[+], D. MÖNKEMEYER*, H.J. MÜCK[+⊕], H.F. NEUMANN*, M. SCHACHTER[+⊗], N. SCHMITZ[×], W. SCHRANKEL[×], B. SCHWARZ*, B.M. SCHWARZSCHILD[×], F. SELONKE[+†], P. SÖDING* and B. WESSELS[+]

Bonn–Hamburg–München–Collaboration

Received 30 August 1973

Abstract: Results on multiplicities, topological cross sections, total particle production cross sections, and correlations between charged particle and π^0 production are presented for pp interactions at 12 and 24 GeV/c incident laboratory momentum. Inclusive production of $\pi^{\pm}$, K_s^0, p, Λ, $\Sigma^{\pm}$ and $\bar{\Lambda}$ is studied; particle spectra are shown in single and double differential form and are compared, in different kinematic regions, with data obtained at other incident momenta and with other beam particles.

1. Introduction

It has become clear in recent years that the investigation of inclusive and exclusive reactions are complementary approaches to uncovering the laws of high-energy multiparticle processes. It may be of particular value to combine both lines of investigation, i.e. to study the various inclusive reactions and to break them down into exclusive components better to understand the features observed. We are performing an experiment where this is being done, and in this paper are presenting the first part of our results on inclusive reactions, namely the multiplicity distributions and single-particle spectra.

The reactions we discuss are

$$p + p \rightarrow C + \text{anything},$$

where $C = \pi^{\pm}$, π^0, K_s^0, p, Λ, $\Sigma^{\pm}$, and $\bar{\Lambda}$, and where we have used two different beam

* Deutsches Elektronen-Synchrotron DESY, Hamburg; II. Institut für Experimentalphysik der Universität Hamburg.
× Max-Planck-Institut für Physik und Astrophysik, München.
+ Physikalisches Institut der Universität Bonn.
± Now at SLAC.
† Now at Deutsches Elektronen-Synchrotron DESY, Hamburg.
⊕ Now at Institut für Informatik der Universitat Hamburg.
⊗ Now at II. Institut für Experimentalphysik der Universität Hamburg.

momenta, $p_{lab} = 12$ GeV/c and 24 GeV/c. Use of a hydrogen bubble chamber as target and detector allows us to detect all charged particles and some of the neutrals emitted, and to identify them in many cases. We have observed and completely measured about 300000 events; the data cover the total available phase space region. Therefore our data supplement the 24 GeV/c data of Allaby et al. [1] who measured $\pi^{\pm}$, $K^{\pm}$, p and $\bar{p}$ spectra with higher statistical precision but in a more restricted kinematic region.

After a discussion of the experimental techniques used (sect. 2), we discuss the results of our measurements on multiplicities, total particle production cross sections and correlations between π^0 and charged particle production (sect. 3). This is followed by a presentation of the pion and K_s^0 spectra (sect. 4) and the baryon spectra (sect. 5) in the form of Lorentz-invariant cross sections as a function of rapidity y, Feynman's scaling variable x and transverse momentum p_T. The spectra are also compared with corresponding ones at other incident momenta. A special study is made of the pion and proton distributions at $x = 0$, i.e. at 90° in the cms (sect. 6) and of the transverse distributions parametrized in terms of the longitudinal mass (sect. 7). Finally a comparison is made with spectra obtained by other incident beam particles in order to study to which extent the inclusive data factorize in the proton fragmentation region (sect. 8). Our main conclusions are then summarized (sect. 9).

Some of the specific aspects of our data (with less statistics) have already been presented [2]. Further inclusive data, e.g. of two-particle distributions, inclusive production of resonances, and polarization data, as well as more detailed investigations using also the breakdown into exclusive reactions, are left for other publications on this experiment.

2. Experimental methods

The data we show come from about 175000 measured events (100000 events) observed in the CERN 2m hydrogen bubble chamber, which was exposed to a proton beam of 12 GeV/c (24 GeV/c) from the CERN proton synchrotron. About half of the film was scanned twice for events of all topologies, the scanning results being then checked in an independent third scan. The cross sections σ_n for the various charged-particle multiplicities n were determined from this scanning procedure, with corrections for scanning loss and for Dalitz pairs from π^0 – decays. The correction for Dalitz pairs was determined from the mass distribution of all pairs of positively and negatively charged tracks, calculated from the measured momenta and assigning the electron mass to the particles. It lies between 2% for low multiplicity events and ~10% for the highest multiplicities at 24 GeV/c. The correction for scanning loss is described later in this chapter. Within the experimental errors, $\sigma_{tot} = \Sigma_n \sigma_n$ as determined in this way agrees with more precise published values from counter experiments [3]. Therefore we normalized our total cross sections σ_{tot} to these more precise values, namely 39.6 mb (38.9 mb) at 12 (24) GeV/c respectively.

Events of all topologies were then measured on Flying Spot Digitizers (FSD), which also gave ionization information on the tracks. The ionization I of a track in the bubble chamber relative to the minimum ionization is given by the relation

$$I = 1 + \frac{m^2}{p^2} = \frac{1}{\beta^2}, \tag{1}$$

where m and p are the mass and the lab momentum, respectively, of the particle. In fig. 1 we show, using only the ionization measurement from the FSD, the distribution

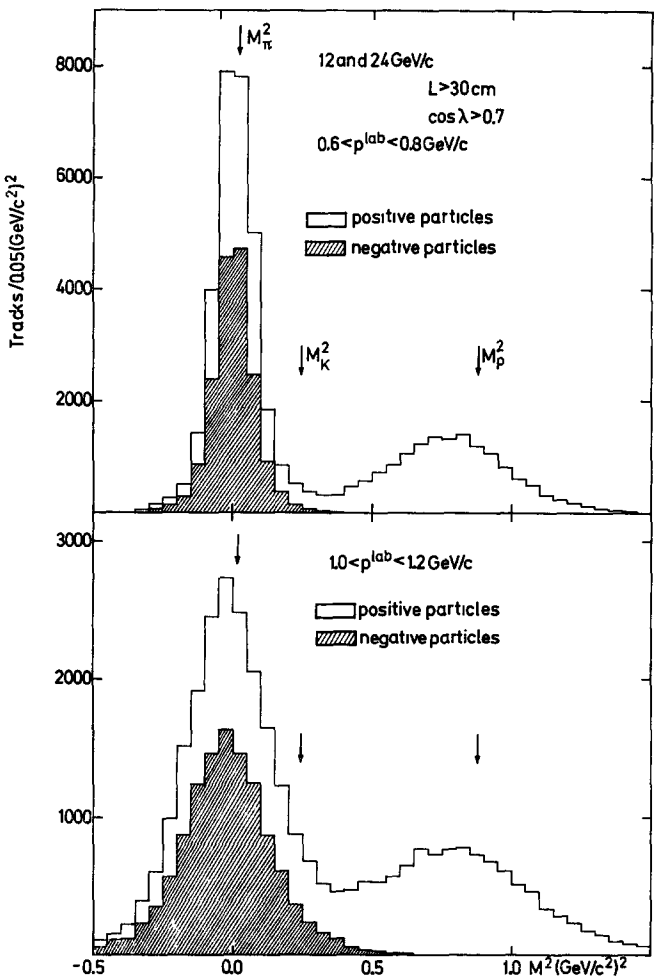

Fig. 1. Distributions of the mass squared from tracks of positively and negatively (shaded histogram) charged particles, obtained from the measured ionization I by the relation $m^2 = p^2\ (I-1)$. Only tracks with length $L>30$ cm and cos $\lambda>0.7$, where λ = dip angle in bubble chamber, are used. The top and bottom figure are for two different momentum regions.

of the mass squared for positive and negative charged particles, obtained by the relation

$$m^2 = p^2(I-1) \tag{2}$$

for two different momentum regions. Only tracks with length $L>30$ cm and with $\cos\lambda>0.7$, where λ is the dip angle, are used. The distribution of m^2 for positive particles shows clear peaks corresponding to the mass squared of the pion and the proton; no peak is visible at the position of the mass squared of the kaon.

With the measured momenta kinematic fits for all possible hypotheses (mass assignments) with no or one neutral particle in the final state were attempted. For the further analysis the elastic events were then removed. The elastic cross section was determined separately; after correction for a scanning loss of 1.92 mb (1.77 mb) at 12 GeV/c (24 GeV/c), it was found to be 9.85 ± 0.2 mb (8.30 ± 0.2 mb) at 12 GeV/c (24 GeV/c), compatible with recently published values [4].

For the inelastic events the ionization information given by the FSD was used to distinguish between different kinematically acceptable hypotheses including the multineutral (unconstrained) hypotheses. Especially for the discrimination between positive pions and protons the combined use of kinematic information on the whole event and the ionization information for each track is very powerful.

Since ambiguities of mass assignment nevertheless remained, we now describe the different methods that were used for the determination of the single particle spectra of the various kinds of particles. In all cases use was made of the forward-backward symmetry of the spectra in the c.m. system due to the symmetry of the initial pp state, in order to detect and correct any possible scanning losses, misidentifications and other biases.

To determine the distributions of the pions and protons we started from the distribution of all charged secondaries except those showing a $K^{\pm}$ or $\Sigma^{\pm}$ decay, or those with a unique strange particle assignment in all hypotheses acceptable from kinematics and ionization. All negative particles were assumed to be pions and all positive particles to be either pions or protons. Pions which go backward in the c.m. system have a low momentum in the lab system such that their ionization distinguishes them from protons; at an incident momentum of 12 GeV/c (24 GeV/c) the lab momentum of a pion with zero longitudinal momentum in the c.m. system is 0.34 GeV/c (0.49 GeV/c) at a transverse momentum $p_T = 0.0$ and is 1.03 GeV/c (1.49 GeV/c) at $p_T = 0.4$ GeV/c. For the π^+ in the backward hemisphere in the c.m. system, the fraction of ambiguities with protons is therefore small and we use only this part of the spectrum. The situation is more difficult for the protons, so that we have to use a subtraction procedure to obtain the proton distribution. This procedure, which we will describe now, is based on the fact that for pp interactions all momentum spectra are symmetric in the c.m. system.

Assuming that all positive particles are either pions or protons, we have

$$N^{\mathrm{pos}}(p_{\parallel}^{\mathrm{lab}}, p_T) = N^{\pi}(p_{\parallel}^{\mathrm{lab}}, p_T) + N^{\mathrm{p}}(p_{\parallel}^{\mathrm{lab}}, p_T), \tag{3}$$

where:

$N^{\mathrm{pos}}(p_{\parallel}^{\mathrm{lab}}, p_{\mathrm{T}})$ = lab spectrum of positive particles,

$N^{\pi}(p_{\parallel}^{\mathrm{lab}}, p_{\mathrm{T}})$ = lab spectrum of π^+, and

$N^{\mathrm{p}}(p_{\parallel}^{\mathrm{lab}}, p_{\mathrm{T}})$ = lab spectrum of protons.

From the experimental point of view, the spectrum of all positive particles can be divided into three parts:

$$N^{\mathrm{pos}}(p_{\parallel}^{\mathrm{lab}}, p_{\mathrm{T}}) = N^{\mathrm{u}}(p_{\parallel}^{\mathrm{lab}}, p_{\mathrm{T}}) + N^{\mathrm{a}}(p_{\parallel}^{\mathrm{lab}}, p_{\mathrm{T}}) + N^{\mathrm{r}}(p_{\parallel}^{\mathrm{lab}}, p_{\mathrm{T}}) \tag{4}$$

where:

$N^{\mathrm{u}}(p_{\parallel}^{\mathrm{lab}}, p_{\mathrm{T}})$ = lab spectrum of unique π^+ that go backward in the c.m. system;

$N^{\mathrm{a}}(p_{\parallel}^{\mathrm{lab}}, p_{\mathrm{T}})$ = lab spectrum of particles that are either π^+ or protons, and go backward in the c.m. system, when transformed as pions;

$N^{\mathrm{r}}(p_{\parallel}^{\mathrm{lab}}, p_{\mathrm{T}})$ = lab spectrum of the remaining particles. These cannot be π^+ going backward in the c.m. system.

Assume first, that there are no ambiguities for backward π^+, i.e. $N^{\mathrm{a}}(p_{\parallel}^{\mathrm{lab}}, p_{\mathrm{T}}) \equiv 0$. Then the lab spectrum of π^+ which go forward in the c.m. system, can be obtained by reflecting track by track all backward π^+ in the c.m. system and transforming them back to the lab system; this transformed spectrum is denoted by $T\{N^{\mathrm{u}}(p_{\parallel}^{\mathrm{lab}}, p_{\mathrm{T}})\}$. The proton spectrum is then simply:

$$N^{\mathrm{p}}(p_{\parallel}^{\mathrm{lab}}, p_{\mathrm{T}}) = N^{\mathrm{r}}(p_{\parallel}^{\mathrm{lab}}, p_{\mathrm{T}}) - T\{N^{\mathrm{u}}(p_{\parallel}^{\mathrm{lab}}, p_{\mathrm{T}})\}. \tag{5}$$

However, the spectrum of ambiguous particles, $N^{\mathrm{a}}(p_{\parallel}^{\mathrm{lab}}, p_{\mathrm{T}})$, cannot be neglected, in particular for large transverse momenta p_{T}. Therefore we assign to the $N^{\mathrm{a}}(p_{\parallel}^{\mathrm{lab}}, p_{\mathrm{T}})$ ambiguous particles a probability α to be a π^+ and a probability $(1-\alpha)$ to be a proton. The probability α is allowed to depend on p_{T}, i.e. $\alpha \equiv \alpha(p_{\mathrm{T}})$.

Then the lab spectrum of the π^+ backward in the c.m. system is given by

$$N^{\pi}_{\mathrm{backward}}(p_{\parallel}^{\mathrm{lab}}, p_{\mathrm{T}}) = N^{\mathrm{u}}(p_{\parallel}^{\mathrm{lab}}, p_{\mathrm{T}}) + \alpha(p_{\mathrm{T}})\, N^{\mathrm{a}}(p_{\parallel}^{\mathrm{lab}}, p_{\mathrm{T}}) \tag{6}$$

and the full proton spectrum is given by

$$N^{\mathrm{p}}(p_{\parallel}^{\mathrm{lab}}, p_{\mathrm{T}}) = N^{\mathrm{r}}(p_{\parallel}^{\mathrm{lab}}, p_{\mathrm{T}}) - T\{N^{\pi}_{\mathrm{backward}}(p_{\parallel}^{\mathrm{lab}}, p_{\mathrm{T}})\} + (1-\alpha(p_{\mathrm{T}}))\cdot N^{\mathrm{a}}(p_{\parallel}^{\mathrm{lab}}, p_{\mathrm{T}}). \tag{7}$$

The probability $\alpha(p_{\mathrm{T}})$ was then determined from the condition that for all p_{T} the total (integrated) c.m. forward and backward proton cross sections must be equal. As an example, we show in fig. 2 the proton distribution $(2E^*/\pi\sqrt{s})\, \mathrm{d}^2\sigma/\mathrm{d}x\mathrm{d}p_{\mathrm{T}}^2$ obtained by this method at 24 GeV/c, integrated over the p_{T} regions 0.0 to 0.4 GeV/c and 0.4 to 0.8 GeV/c; shown as shaded histograms are the subtracted distribution (second term in eq. (7)) and the fraction of the distribution due to tracks which are ambiguous with

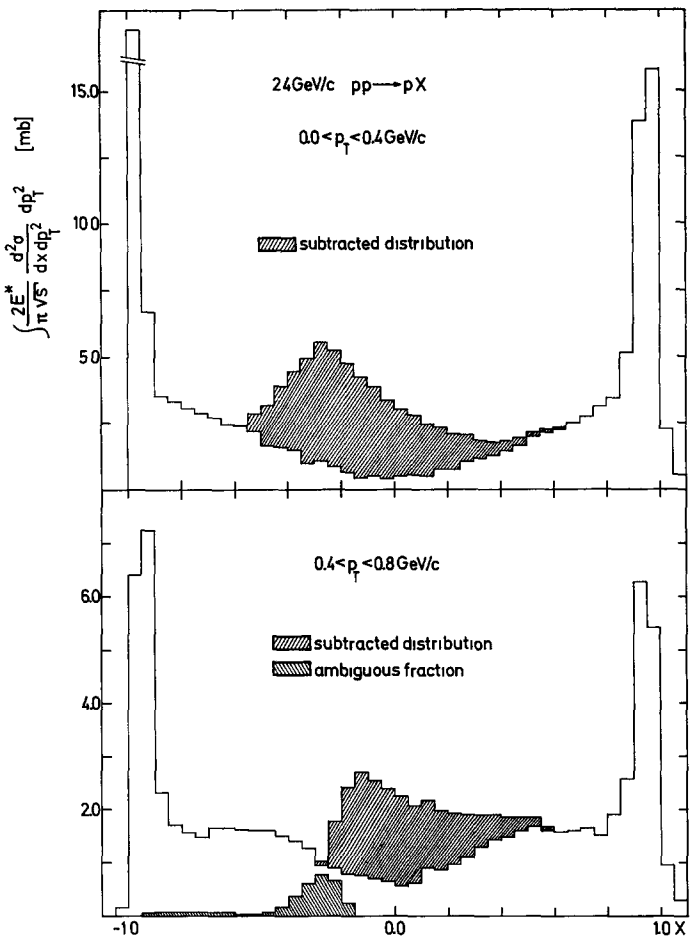

Fig. 2. Invariant cross section *versus* x for p in two p_T regions, obtained by the method described in the text. The shaded histograms are the subtracted distribution and the fraction from ambiguous tracks respectively.

backward pions. The proton distribution is symmetric within the statistical errors which demonstrates the applicability of the method.

From an analysis of the inelastic proton spectra so obtained, we determined a scanning loss of 0.2 mb (0.31 mb) at 12 GeV/c (24 GeV/c) for protons with small laboratory momenta in events with two charged particles. The spectra were corrected for this effect. In the pion spectra, there is a loss at laboratory momenta below 50 MeV/c which was attributed to the measuring procedure (not scanning loss).

The estimated systematic error in the $\pi^{\pm}$ and p longitudinal momentum spectra due to contamination by charged kaons and other less abundantly produced particles,

is about 2% to 3%. For π^+ and p the systematic error increases with transverse momentum to about 10% for transverse momenta above 0.4 GeV/c.

For π^0's only the average multiplicity was determined as a function of the number of charged particles. The e^+e^- pair production vertices were measured on about half of the film. The π^- and π^+ spectra were used to simulate the shape of a π^0 spectrum, and from this the expected angular distribution of the pair production vertices was calculated using the known pair production cross section in hydrogen [5]. This was then compared with the measured distribution of the vertices. In this way the π^0 detection efficiency could be determined, assuming two photons per π^0.

To obtain the spectra of the neutral strange particles K_s^0, Λ and $\bar{\Lambda}$ a cut-off length of 1 cm for the observed V^0 and the usual weight factor correcting for this cut-off and for decays outside the fiducial volume, were used. For about 5% of the observed neutral strange particles no unambiguous distinction between K_s^0 and Λ was possible. From various checks it was concluded that these events were Λ decays [6]. The principal reason was that the decay distribution of the uniquely identified sample of K_s^0 is symmetric; on the other hand, for the ambiguous events the transverse momentum distribution with respect to the line of flight of the V^0 shows a peak at the same p_T value of 0.1 GeV/c as the unambiguous Λ decays. A correction of the Λ spectrum for loss of events misidentified as e^+e^- pairs, was also made. Furthermore, all possible $\bar{\Lambda}$ events were checked for this interpretation on the scanning table.

In the determination of the $\Sigma^\pm$ spectra, corrections were made for a loss of particles with decay length below 10 cm. Only the better identified $n\pi^+$ decay mode was used for the Σ^+ with a correction of the cross section for the $p\pi^0$ decay.

All strange particle production cross sections were also corrected for unobserved decay modes. Finally, for all kinds of particles the slightly different pass rates through the measuring and analysis system of events with different topologies (prong numbers) has been taken into account.

3. Integrated cross sections and multiplicities

Table 1 lists the topological cross sections σ_n for the various charged-particle multiplicities n. The errors contain statistical uncertainties as well as systematic normalization uncertainties and uncertainties from the loss of events with particles of very small laboratory momentum. In addition table 1 contains the values of $\sigma_{inel} = \Sigma_n \sigma_n$, the elastic cross section σ_{el} and the values of the total cross section σ_{tot}, which were used for the overall normalization.

The average particle multiplicity $\langle n \rangle$, the dispersion D^2 and $f_2 = D^2 - \langle n \rangle$ are given in table 2 both for all charged particles and the negatively charged particles. Here $\langle n \rangle$ is defined to be the average multiplicity per inelastic collision. The π^0 multiplicity $\langle n_{\pi^0}(n) \rangle$ as a function of the number n of charged particles at 12 and 24 GeV/c is shown in fig. 3, together with other bubble chamber data at 12.4 and 205 GeV/c [7]

Table 1

Cross sections σ_n for the various charged-particle multiplicities n (topological cross sections) and elastic, inelastic and total cross sections

	Cross section values (mb)	
	12 GeV/c	24 GeV/c
$\sigma_{2,\,\mathrm{inel}}$	12.70 ±0.25	8.70 ±0.25
σ_4	13.20 ±0.10	12.55 ±0.10
σ_6	3.45 ±0.04	6.71 ±0.07
σ_8	0.381 ±0.013	2.17 ±0.04
σ_{10}	0.013 ±0.002	0.404 ±0.016
σ_{12}		0.041 ±0.005
σ_{14}		0.005 ±0.002
σ_{16}		0.002 ±0.001
σ_{inel}	29.75 ±0.25	30.6 ±0.25
σ_{el}	9.85 ±0.20	8.30 ±0.20
σ_{tot}	39.6 ±0.1	38.9 ±0.1

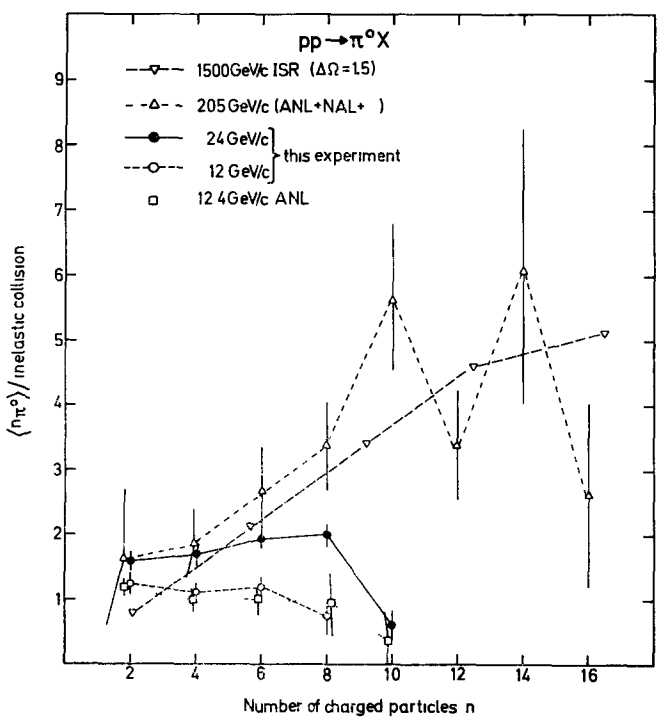

Fig. 3. Average π^0 multiplicity $\langle n_{\pi^0}(n)\rangle$ as a function of the number n of charged particles in the final state at 12 and 24 GeV/c, compared with data from other experiments. The ISR data refer to the indicated range of solid angle.

Table 2
Moments of inelastic charged particle multiplicity distributions

	12 GeV/c	24 GeV/c
$\langle n_{ch} \rangle$	3.43 ±0.03	4.25 ±0.03
$D^2 = \langle n_{ch}^2 \rangle - \langle n_{ch} \rangle^2$	2.05 ±0.03	3.68 ±0.06
$f_2 = D^2 - \langle n_{ch} \rangle$	−1.38 ±0.04	−0.57 ±0.07
$\langle n_- \rangle = \frac{1}{2} \langle n_{ch} \rangle - 1$	0.715 ±0.015	1.125 ±0.015
$D_-^2 = \frac{1}{4} D^2$	0.51 ±0.01	0.920 ±0.015
$f_{2--} = \frac{1}{4} f_2 - \frac{1}{2} \langle n_{ch} \rangle + 1$	−0.20 ±0.02	−0.20 ±0.02
$f_{20-} = \langle n_0 n_- \rangle - \langle n_0 \rangle \langle n_- \rangle$	−0.03 ±0.08	0.03 ±0.12

and data obtained at the CERN intersecting storage rings [8]. At our energies the variation of $\langle n_{\pi^0}(n) \rangle$ with n is small; the decrease of $\langle n_{\pi^0} \rangle$ at the largest values of n is probably a phase-space effect.

The integrated single particle inclusive cross sections $\sigma_c = \langle n_c \rangle \cdot \sigma_{inel}$ for c = π^-, π^0, π^+, K^0 or $\bar{K}^0$, p, Λ, $\bar{\Lambda}$, Σ^- and Σ^+ are given in table 3. The Λ and $\bar{\Lambda}$ cross sections include the $\Lambda(\bar{\Lambda})$ from $\Sigma^0(\bar{\Sigma}^0)$ decays.

Table 3
Integrated single particle inclusive cross sections $\sigma_c = \langle n_c \rangle \sigma_{inel}$, where $\langle n_c \rangle$ = average multiplicity of particle c per inelastic collision

	Cross sections values (mb) 12 GeV/c	24 GeV/c
π^-	21.1 ±0.4	33.8 ±0.6
π^0	35.2 ±2.4	53.5 ±3.1
π^+	42.7 ±0.7	56.8 ±0.9
K^0 or $\bar{K}^0$[a]	1.15 ±0.03	2.51 ±0.06
p	37.5 ±0.6	37.9 ±0.6
Λ[b]	1.12 ±0.03	1.76 ±0.06
$\bar{\Lambda}$[b]	0.003 $^{+0.001}_{-0.002}$	0.021 $^{+0.004}_{-0.010}$
Σ^-	0.16 ±0.01	0.28 ±0.02
Σ^+	0.49 ±0.02	0.85 ±0.03

[a] Since only K_s^0 were detected with non-negligible probability, these numbers were obtained as twice the production cross sections for K_s^0.
[b] The Λ and $\bar{\Lambda}$ cross sections include $\Lambda(\bar{\Lambda})$ from $\Sigma^0(\bar{\Sigma}^0)$ decays.

4. Meson spectra

In this section we present cross sections for the inclusive reactions

$$pp \to \pi^{\pm} X, \tag{8}$$

$$pp \to K_s^0 X, \tag{9}$$

where X stands for "anything".

We first define the notation. Let p_T be the transverse, $p_\parallel$ the longitudinal momentum, and $E = \sqrt{p_\parallel^2 + p_T^2 + m^2}$ the energy of the observed final-state particle. Furthermore,

$$y = \tfrac{1}{2} \ln[(E + p_\parallel)/(E - p_\parallel)] = \tanh^{-1}(p_\parallel/E)$$

is the longitudinal rapidity, and $x = 2p_\parallel^*/\sqrt{s}$ the Feynman scaling variable, defined in terms of the longitudinal momentum $p_\parallel^*$ of the meson in the center-of-momentum

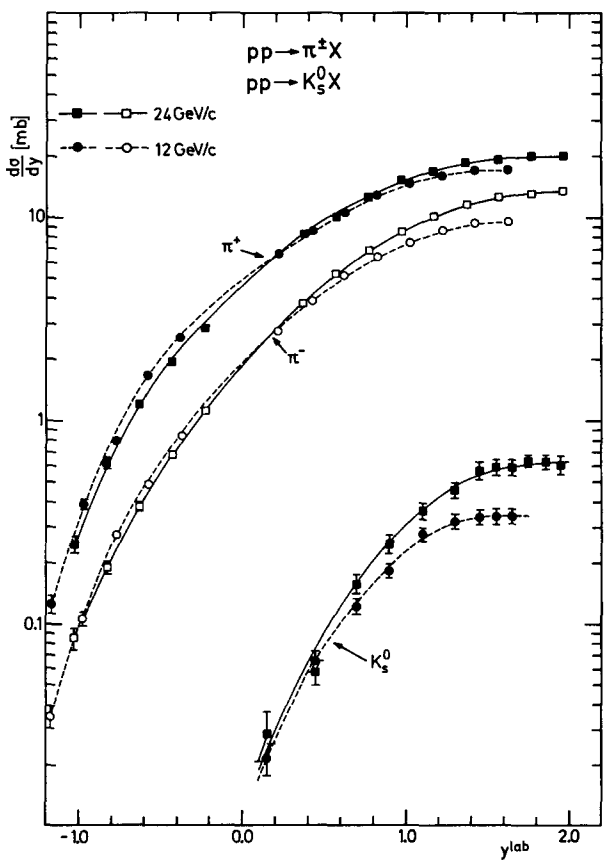

Fig. 4. Invariant cross section *versus* y^{lab} for inclusive $\pi^{\pm}$ and K_s^0 production. The curves are hand-drawn, to guide the eye. Near $y^{lab} = 0$ the cross sections could not be well measured.

system of the reaction, and of the total energy $\sqrt{s}$ of the final state in the cms. The Lorentz-invariant differential cross section for unpolarized incident particles is

$$\frac{d^3\sigma}{dp/E} \equiv \frac{1}{\pi}\frac{d^2\sigma}{dy\,dp_T^2} \equiv \frac{2E^*}{\pi\sqrt{s}}\frac{d^2\sigma}{dx\,dp_T^2}. \tag{10}$$

Quantities with an asterisk are cms quantities. Due to the forward-backward symmetry of the initial state, all longitudinal distributions are symmetric about $x = y^* = 0$, corresponding to $y^{lab} = 1.62$ (at 12 GeV/c incident momentum) or $y^{lab} = 1.97$ (at 24 GeV/c).

We start with single-differential spectra, i.e. the invariant cross section as a function of y^{lab}, x and p_T, which are obtained by integrating (10) over the respective other variable. Figs. 4-6 show these distributions for $\pi^\pm$ and K_s^0 at both incident momenta of 12 and 24 GeV/c. The curves in these figures are hand-drawn to guide the eye.

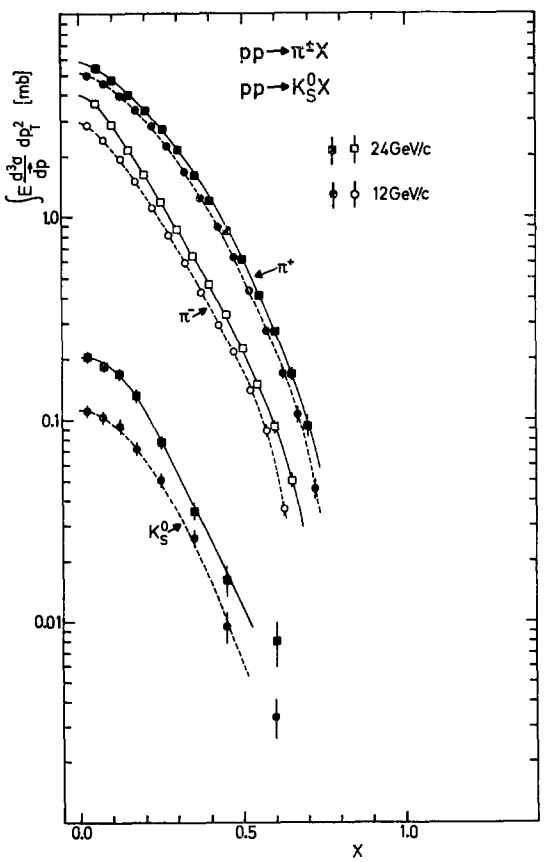

Fig. 5. Invariant cross section *versus* x for inclusive $\pi^\pm$ and K_s^0 production. The curves are hand-drawn, to guide the eye.

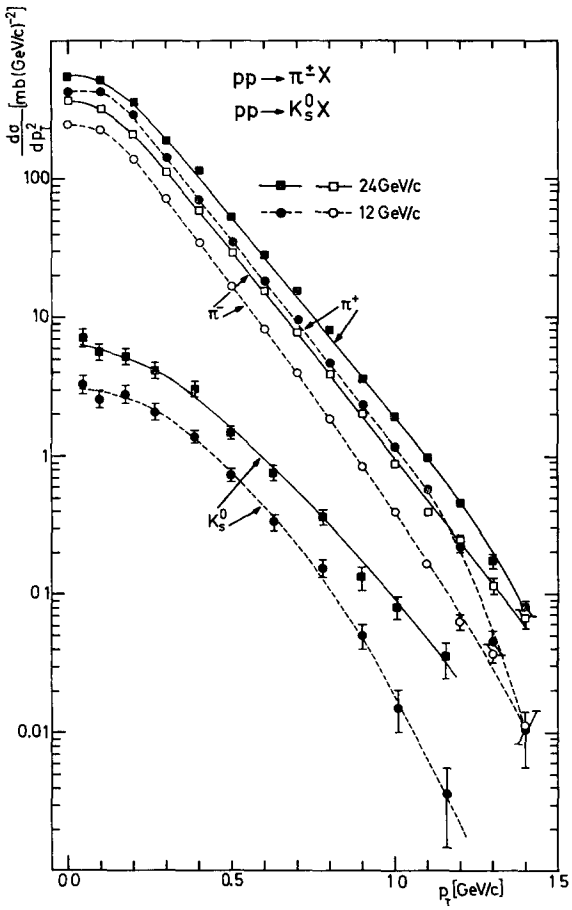

Fig. 6. Invariant cross section *versus* p_T for inclusive $\pi^{\pm}$ and K_s^0 production. The curves are hand-drawn, to guide the eye.

From fig. 4 it is apparent that the increase of the total (integrated) pion production cross section between 12 and 24 GeV/c (compare table 3) is largely a result of the increase in the available longitudinal phase space (i.e. the y^{lab} range available); on the other hand for K_s^0 production energy-dependent dynamic effects are manifest in that even at fixed y^{lab} values there is up to a factor of 2 increase of the invariant cross section between 12 and 24 GeV/c. This increase is largest in the central region (near $x = y^* = 0$), while in the fragmentation regions, at small values of $|y^{lab}|$, both the $\pi^{\pm}$ and the K_s^0 spectra at fixed y^{lab} are independent of incident momentum between 12 and 24 GeV/c within better than 20%. It is also interesting to note that the $\pi^{\pm}$ spectra are falling (rising) with incident momentum in the fragmentation (central) regions while the K_s^0 cross section is rising everywhere. Finally, we observe that the

K_s^0/π^+ ratio is 1/30 near the central region but drops to $\sim\frac{1}{100}$ in the fragmentation region (at 24 GeV/c), and that it is much larger at large p_T than at small p_T. (The transverse momentum dependences will be further discussed in sect. 7.)

The y^{lab} distributions for $\pi^\pm$ production at fixed multiplicities of the charged particles in the final state (prong number) are shown in figs. 7 and 8. Large variations are

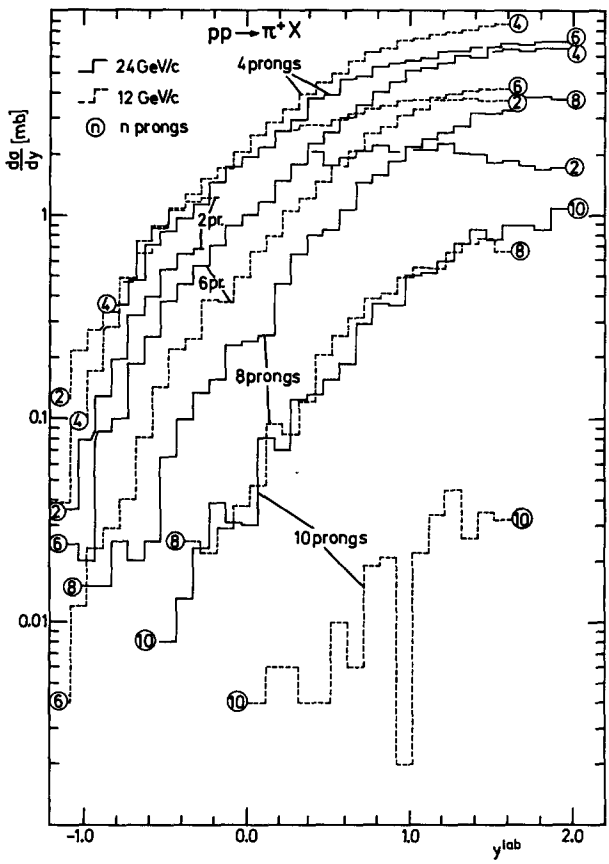

Fig. 7. Invariant cross section *versus* y^{lab} for π^+ for various multiplicities of the charged particles in the final state (prong number). Near $y^{lab} = 0$ the 2-prong cross sections could not be well measured.

observed everywhere when the incident momentum changes from 12 to 24 GeV/c, but these variations conspire such that for the total production cross section (summed over all multiplicities) very little change remains. Note also that the two-prong cross section (which exists for π^+ only) has at 24 GeV/c a dip in the central region, indicating that pions from events with only two (positive) charged particles are fragmentation products.

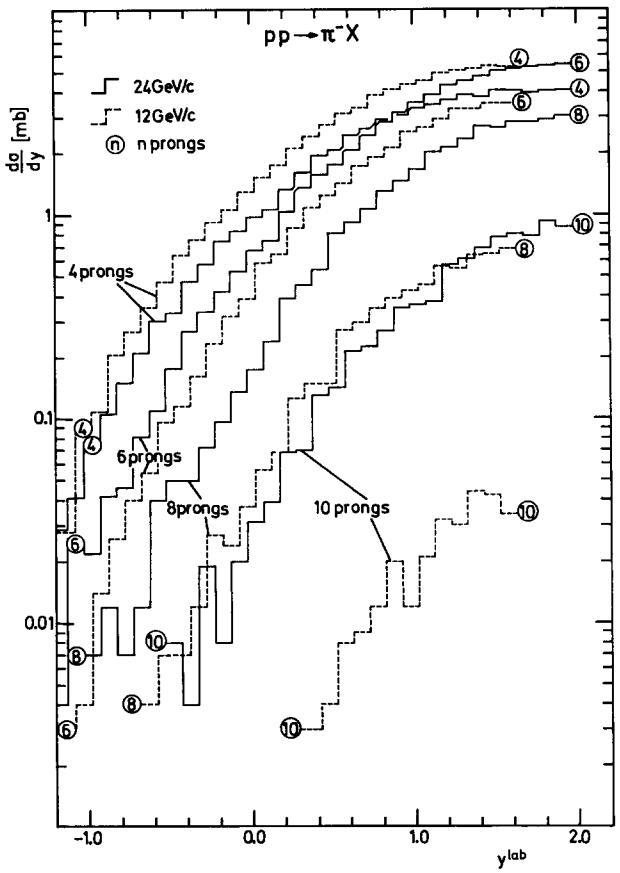

Fig. 8. Invariant cross section *versus* y^{lab} for π^- for various multiplicities of the charged particles in the final state (prong number).

Next we present $\pi^\pm$ spectra in double-differential form as functions of y^{lab} and x for different fixed values of p_T (figs. 9 and 10). To obtain cross section values at fixed values of p_T, use was made of the fact that, in small regions of y^* and p_T, an expression of the factorized form

$$\exp(-Ap_T^2 - Bp_T^4) \cdot \exp(-Cy^* - Dy^{*2})$$

gives a good fit to the data. Expressions of this form were fitted to the experimental invariant cross section $(1/\pi)\mathrm{d}^2\sigma/\mathrm{d}y^*\mathrm{d}p_T^2$ in regions 0.2 GeV/c wide in p_T and 0.2 wide in y^*. The fitted expressions were used to obtain interpolated cross section values at the center of each region. The cross section values obtained in this way are plotted as curves in figs. 9 and 10. Numerical values of the cross sections are given in tables 4a and 4b in steps of 0.2 in y^* and 0.2 GeV/c in p_T; these values are shown in figs. 9 and 10

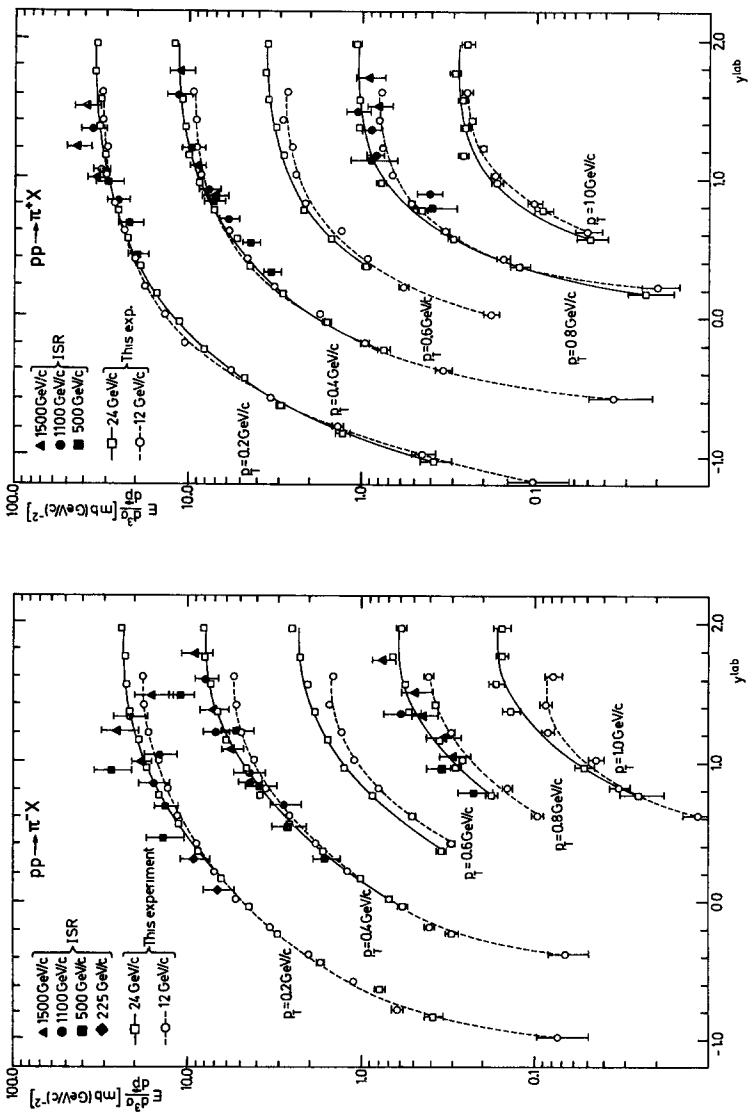

Fig. 9. Invariant cross section *versus* y^{lab} for $\pi^{\pm}$ at different values of p_T (see text).

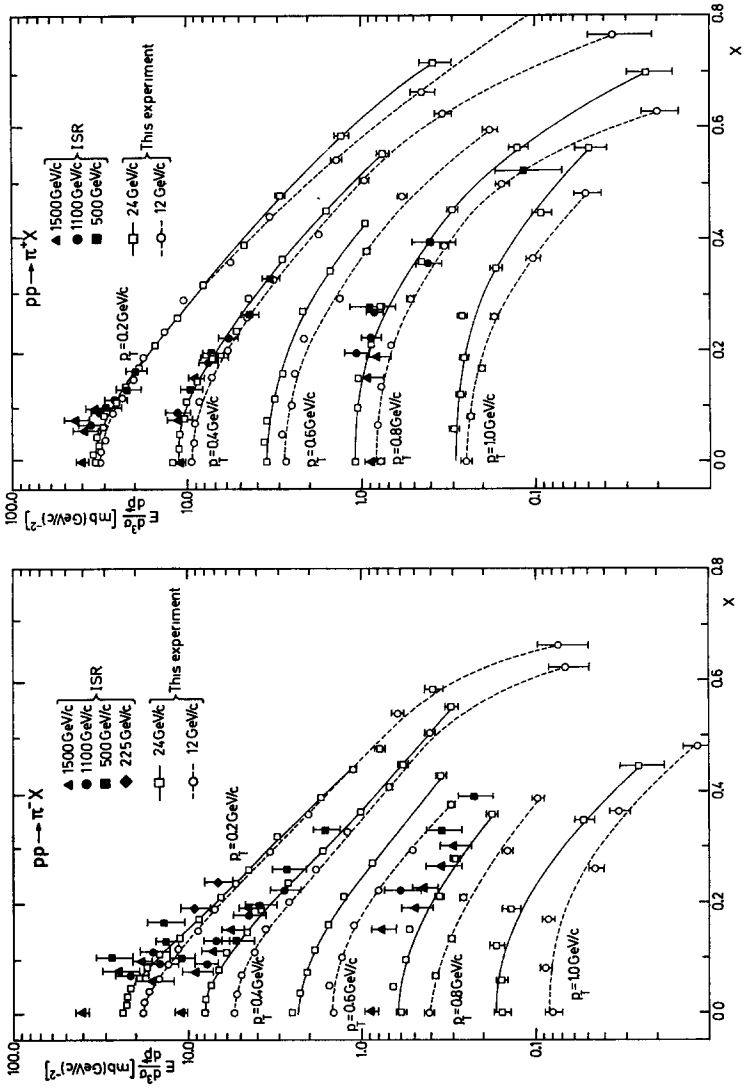

Fig. 10. Invariant cross section *versus* x for $\pi^{\pm}$ at different values of p_T (see text).

as (open) symbols with error bars. The full symbols are cross section values measured at the CERN intersecting storage rings at much higher equivalent incident momenta [9].

It appears from figs. 9 and 10 that the increase in the $\pi^{\pm}$ differential production cross sections between 24 GeV/c and ISR energies, is not larger than that between 12 and 24 GeV/c incident momentum. In general the energy independence appears to be somewhat less when the data are compared at fixed p_T and y^{lab}, rather than at fixed p_T and x (note e.g. the $p_T = 0.8$ GeV/c data for π^-).

For the K_s^0 distributions, due to the smaller number of observed events we cannot present the data in the same double-differential form as for pions in figs. 9 and 10.

Table 4a

Inclusive π^- cross sections $Ed^3\sigma/dp$ (mb (GeV/c)$^{-2}$). Of each pair of numbers, the upper one is for 12 GeV/c, the lower one for 24 GeV/c incident momentum

y^* \ p_T	0.2 (GeV/c)	0.4 (GeV/c)	0.6 (GeV/c)	0.8 (GeV/c)	1.0 (GeV/c)
0.0	18.04 ±0.31	5.43 ±0.12	1.46 ±0.05	0.413 ±0.023	0.079 ±0.009
	23.58 ±0.51	7.99 ±0.21	2.50 ±0.09	0.593 ±0.037	0.156 ±0.017
0.2	17.71 ±0.21	5.23 ±0.08	1.53 ±0.04	0.377 ±0.015	0.087 ±0.007
	22.59 ±0.33	7.95 ±0.14	2.24 ±0.06	0.659 ±0.026	0.156 ±0.012
0.4	16.66 ±0.20	4.90 ±0.08	1.30 ±0.04	0.305 ±0.014	0.084 ±0.007
	22.33 ±0.33	7.34 ±0.13	2.05 ±0.06	0.559 ±0.024	0.168 ±0.018
0.6	14.60 ±0.19	4.13 ±0.07	1.11 ±0.03	0.262 ±0.013	0.045 ±0.005
	21.40 ±0.32	6.70 ±0.12	1.86 ±0.05	0.533 ±0.024	0.139 ±0.017
0.8	12.96 ±0.18	3.56 ±0.07	0.801 ±0.024	0.145 ±0.010	0.033 ±0.005
	18.95 ±0.30	6.01 ±0.12	1.56 ±0.05	0.354 ±0.018	
1.0	11.43 ±0.17	2.61 ±0.06	0.512 ±0.019	0.097 ±0.008	0.011 ±0.003
	17.27 ±0.29	4.58 ±0.10	1.26 ±0.04	0.290 ±0.018	0.052 ±0.007
1.2	8.79 ±0.14	1.84 ±0.05	0.306 ±0.016		
	14.47 ±0.26	3.82 ±0.09	0.873 ±0.034	0.179 ±0.014	0.025 ±0.008
1.4	7.03 ±0.13	1.21 ±0.04			
	11.21 ±0.23	2.66 ±0.08			
1.6	5.34 ±0.12	0.694 ±0.028			
	8.67 ±0.20	1.67 ±0.06	0.350 ±0.023		
1.8	3.36 ±0.09	0.407 ±0.027			
	6.42 ±0.17	1.01 ±0.05			
2.0	2.01 ±0.07	0.066 ±0.018			
	4.43 ±0.14	0.580 ±0.035			
2.2	1.12 ±0.06				
	3.03 ±0.12	0.304 ±0.026			
2.4	0.622 ±0.048				
	1.72 ±0.09				
2.6	0.073 ±0.024				
	0.788 ±0.054				
2.8	0.387 ±0.047				

Table 4b

Inclusive π^+ cross sections $Ed^3\sigma/dp$ (mb (GeV/c)$^{-2}$). Of each pair of numbers, the upper one is for 12 GeV/c, the lower one for 24 GeV/c incident momentum

y^* \ p_T	0.2 (GeV/c)	0.4 (GeV/c)	0.6 (GeV/c)	0.8 (GeV/c)	1.0 (GeV/c)
0.0	31.31 ±0.56	9.41 ±0.22	2.77 ±0.09	0.774 ±0.035	0.251 ±0.017
	33.43 ±0.82	12.09 ±0.35	3.52 ±0.13	1.09 ±0.06	0.250 ±0.021
0.2	31.27 ±0.39	9.09 ±0.14	2.86 ±0.07	0.800 ±0.023	0.234 ±0.011
	34.61 ±0.57	11.03 ±0.21	3.61 ±0.09		0.292 ±0.017
0.4	29.38 ±0.37	8.98 ±0.14	2.52 ±0.06	0.766 ±0.025	0.202 ±0.010
	31.95 ±0.54	10.93 ±0.21	3.48 ±0.09	1.04 ±0.04	0.266 ±0.014
0.6	29.78 ±0.40	8.49 ±0.14	2.41 ±0.06	0.673 ±0.028	0.172 ±0.010
	32.80 ±0.55	10.47 ±0.21	3.13 ±0.09	1.05 ±0.04	0.255 ±0.014
0.8	26.64 ±0.38	7.22 ±0.13	2.12 ±0.06	0.522 ±0.024	0.103 ±0.010
	30.24 ±0.54	9.99 ±0.21	2.82 ±0.09	0.871 ±0.038	0.263 ±0.016
1.0	23.33 ±0.37	5.82 ±0.12	1.31 ±0.04	0.334 ±0.019	0.051 ±0.010
	29.77 ±0.54	8.70 ±0.19		0.776 ±0.039	0.168 ±0.013
1.2	20.20 ±0.34	4.55 ±0.11	0.931 ±0.036	0.154 ±0.014	
	25.27 ±0.50	7.16 ±0.17	2.17 ±0.08	0.451 ±0.027	0.092 ±0.012
1.4	17.71 ±0.32	3.16 ±0.09	0.579 ±0.033	0.020 ±0.005	
	22.25 ±0.48	5.24 ±0.14	1.51 ±0.06	0.300 ±0.022	0.049 ±0.011
1.6	13.53 ±0.26	1.74 ±0.06	0.181 ±0.018		
	18.88 ±0.40	4.41 ±0.13	0.946 ±0.049	0.125 ±0.017	
1.8	10.47 ±0.23	0.958 ±0.049			
	15.22 ±0.38	2.84 ±0.11		0.023 ±0.007	
2.0	5.64 ±0.16	0.340 ±0.037			
	11.30 ±0.30	1.580 ±0.079			
2.2	3.34 ±0.12	0.035 ±0.014			
	8.03 ±0.26	0.748 ±0.064			
2.4	1.38 ±0.10				
	4.69 ±0.19				
2.6	0.445 ±0.070				
	2.93 ±0.16				
2.8	0.105 ±0.040				
	1.29 ±0.13				
3.0					
	0.382 ±0.080				

Nevertheless, in fig. 11 and 12 we show the y^{lab} and x distributions of the K_s^0 for various regions of the transverse momentum p_T. The curves here are eyeball fits to guide the eye. Comparison with K_s^0 data at higher energy is made in figs. 13 and 14 where the x and p_T^2 distributions are shown together with data obtained at NAL at 205 GeV/c incident momentum [10]. While the shape of both distributions does not change much between 12 and 205 GeV/c, there is a substantial increase, by a factor of about 2, in cross section.

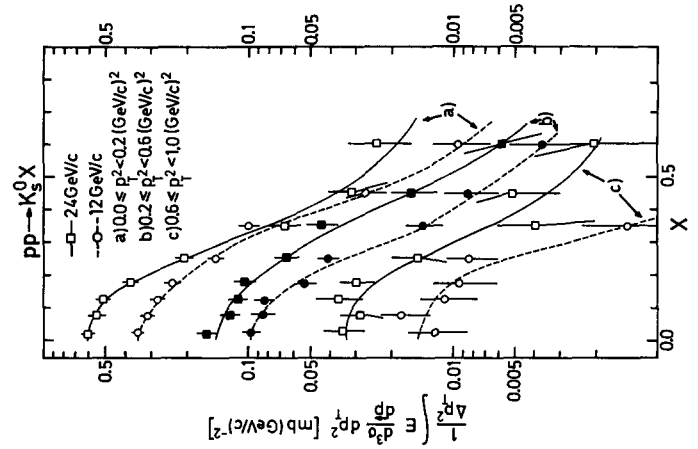

Fig. 12. Invariant cross section *versus* x for K_s^0 in different regions of p_T. The curves are hand-drawn to guide the eye.

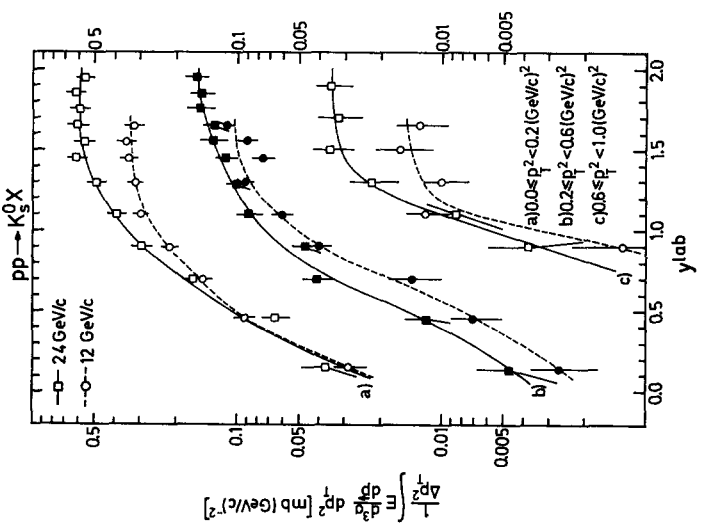

Fig. 11. Invariant cross section *versus* y^{lab} for K_s^0 in different regions of p_T. The curves are hand-drawn to guide the eye.

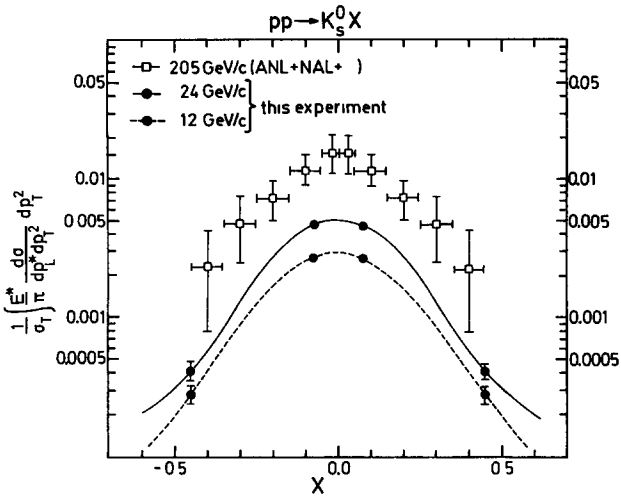

Fig. 13. Invariant cross section *versus* x for K_s^0, divided by the asymptotic pp total cross section, compared with data at 205 GeV/c.

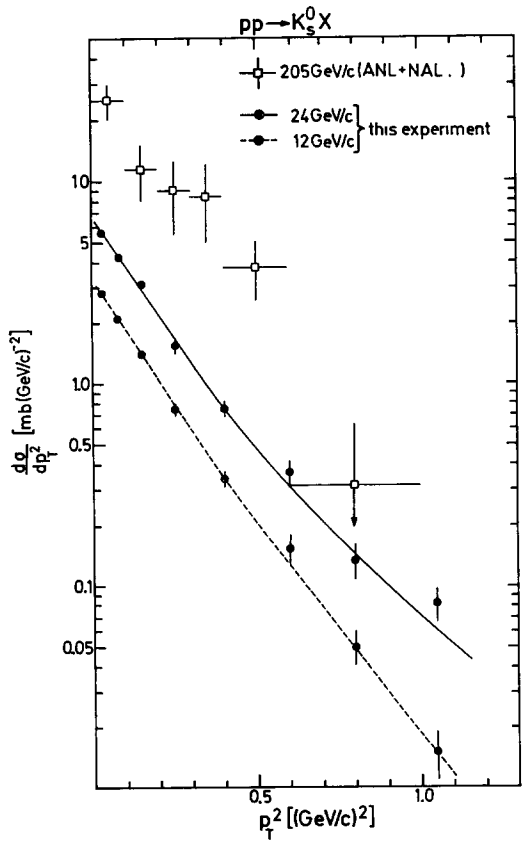

Fig. 14. Invariant cross section *versus* p_T^2 for K_s^0, compared with data at 205 GeV/c.

5. Baryon spectra

We now present cross sections for the inclusive reactions

$pp \to pX$, ΛX, $\Sigma^+ X$, $\Sigma^- X$ and $\bar{\Lambda} X$,

where again X stands for "anything" (except a single proton, i.e. excluding elastic scattering). The notations and definitions are the same as in sect. 4.

Single-differential spectra as a function of y^{lab}, x and p_T are shown in figs. 15-17. Again, the curves on these figures are hand-drawn to guide the eye. The proton distributions show a clear leading-particle effect and a decrease of the inclusive cross section with increasing incident momentum (in particular in the central region) while the hyperon cross sections increase. The invariant cross section as a function of p_T of the Σ show a slower decrease with p_T than the p and Λ distributions.

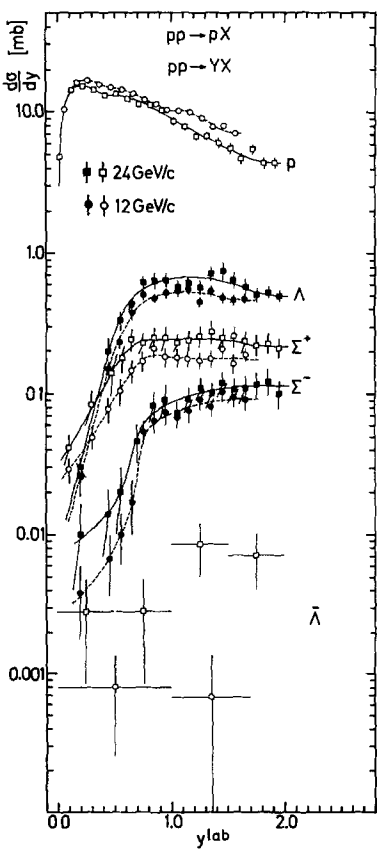

Fig. 15. Invariant cross section *versus* y^{lab} for p, Λ (including Λ from Σ^0 decay), Σ^+, Σ^- and $\bar{\Lambda}$. The curves are hand-drawn to guide the eye.

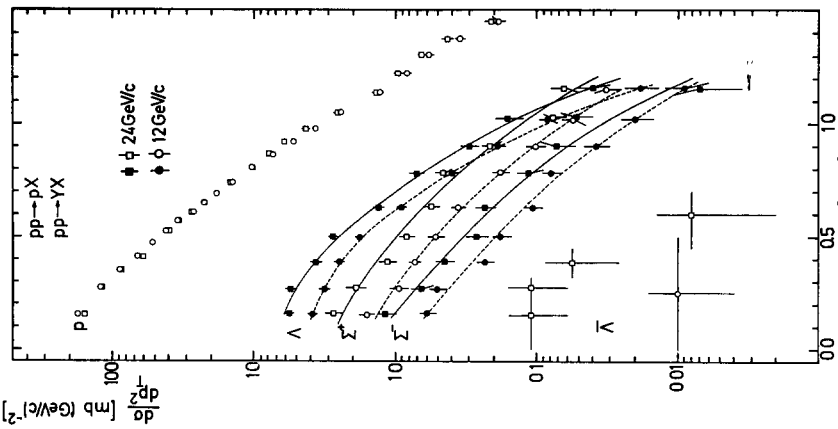

← Fig. 16. Invariant cross section *versus* x for p, Λ (including Λ from Σ^0 decay), Σ^+, Σ^- and $\bar{\Lambda}$. The curves are hand-drawn to guide the eye.

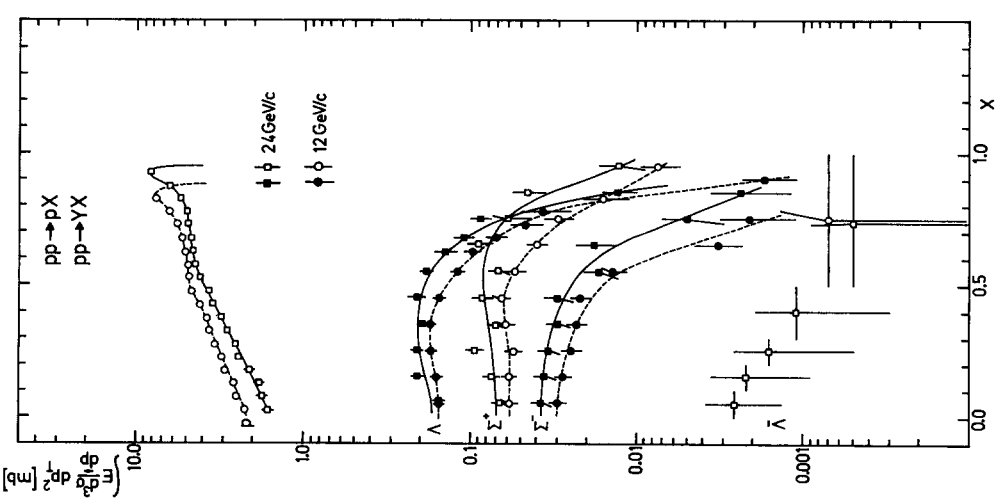

Fig. 17. Invariant cross section *versus* → p_T for p, Λ (including Λ from Σ^0 decay), Σ^+, Σ^- and $\bar{\Lambda}$. The curves are hand-drawn to guide the eye.

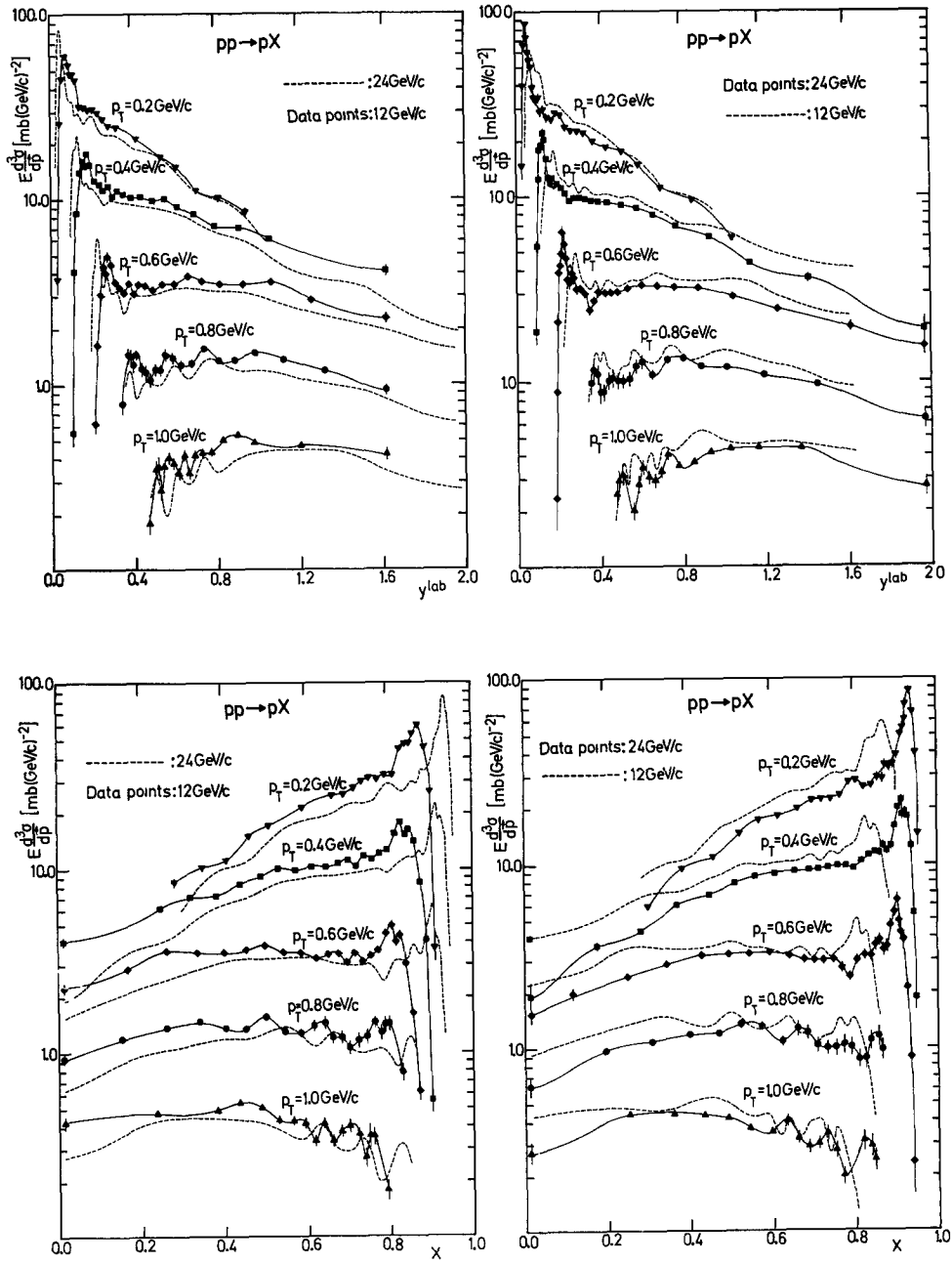

Fig. 18. Invariant cross section *versus* y^{lab} (a) and x (b) for p at different fixed values of p_T. The solid lines are interpolating curves through the data points at one energy, the dashed curves are the interpolating curves at the other energy.

The invariant cross sections $d^3\sigma/(dp/E)$ for the reaction $pp \to pX$ are shown in fig. 18 in double-differential form, i.e. as a function of y^{lab} or x at fixed values of p_T. They have been obtained in the following way. For bins in missing mass squared M_x^2 with respect to the proton, exponentials in momentum transfer t were fitted to the experimental invariant cross section expressed as a function of M_x^2 and t,

$$\frac{d^3\sigma}{dp/E} = \frac{2p^*_{inc}\sqrt{s}}{\pi}\frac{d^2\sigma}{dM_x^2 dt} = a\exp(bt+ct^2)$$

for two t regions covering the p_T range 0.2 to 1.0 GeV/c. From the fitted expressions, cross sections in steps of 0.2 GeV/c in p_T were obtained as a function of y^{lab} and x. The reason for obtaining the y and x distributions from the M_x^2 and t distribution is of course the observed resonance structure in M_x^2 at low missing masses.

A detailed discussion of the double-differential cross section for inclusive p production, of the role of diffractive processes and a comparison with data at higher incident momenta, will be the subject of another forthcoming paper. Here, we mention only that the first maximum (from the edge of phase space at $x \simeq 1$ or $y^{lab} \approx 0$) at small p_T corresponds to the N*(1470) in the missing mass M_x. In the present context, we continue with a comparison of the Λ production cross sections with those recently obtained in an experiment at NAL [10]. Figs 19 and 20 show the x and p_T^2 distributions for the inclusive reaction $pp \to \Lambda X$ at 6.6 [11], 12, 24 and 205 GeV/c. Although the errors of the 205 GeV/c data are still rather large, it appears that they differ signifi-

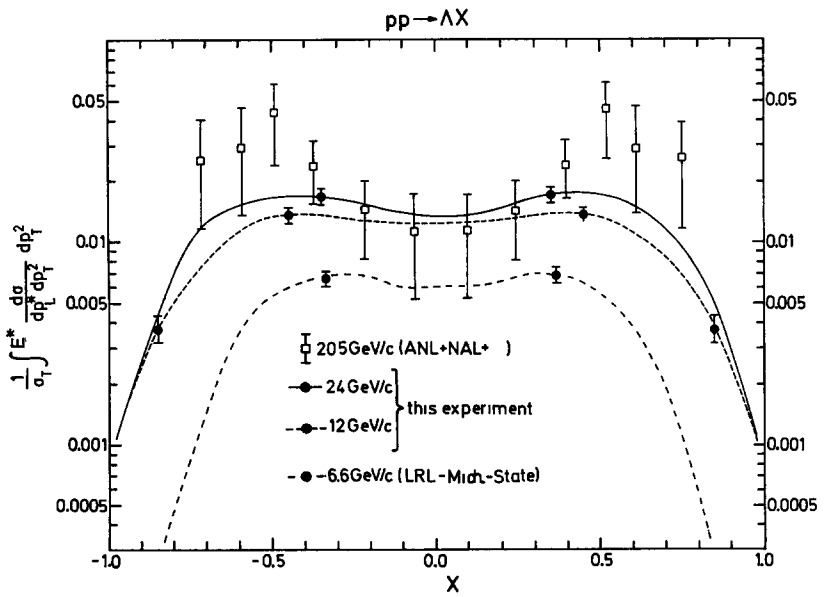

Fig. 19. Invariant cross section *versus* x for Λ, divided by the asymptotic pp total cross section, compared with data at other energies. Only a few points are shown to indicate the size of the errors.

cantly from the 24 GeV/c data, mainly in that a more pronounced central dip in the x distribution seems to appear. This would point to a fragmentation-type production mechanism for the Λ's at this energy.

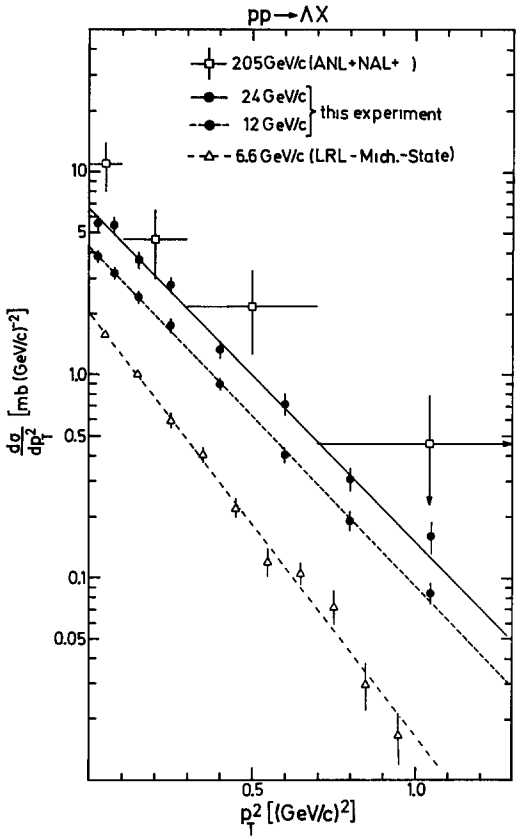

Fig. 20. Invariant cross section *versus* p_T^2 for Λ, compared with data at other energies.

6. Spectra around 90° in the center of mass system

In this section the s and p_T dependence of the invariant cross section for pions and protons in the central region is studied. In particular, we compare, at 90° in the c.m. system, our data with the data obtained at the CERN intersecting storage rings.

To obtain cross sections at 90° (or at c.m.s. rapidity $y^* = 0$), a method analogous to that described in sect. 4 was used. The expression

$$E\frac{d^3\sigma}{dp} \equiv \frac{1}{\pi}\frac{d^2\sigma}{dy^* dp_T^2} = \left(\frac{1}{\pi}\frac{d^2\sigma}{dy^* dp_T^2}\right)_{y^*=0} \exp(-Dy^{*2}) \tag{11}$$

was fitted in p_T bins of 0.05 GeV/c to the experimental invariant cross section for $|y^*| < 0.4$. In this region of y^*, eq. (11) gives a very good fit to the data. Every two bins in p_T were combined to give one cross section value, assuming an exponential behaviour in p_T of the cross section over the two bins. Adjacent data are thus not statistically correlated. An exception is the point at $p_T = 0$, which was extrapolated from the p_T bins 0 to 0.05 GeV/c and 0.05 to 0.1 GeV/c.

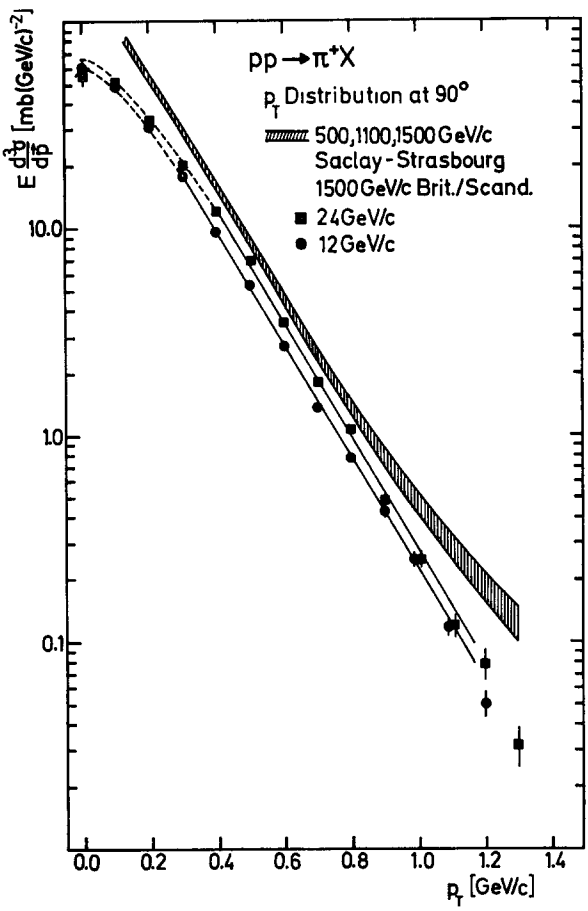

Fig. 21. Invariant cross section at 90° in the c.m. system for π^+ as a function of p_T. The solid straight line is an exponential fit in p_T, the dashed curve is an exponential fit in the generalized longitudinal mass μ.

The invariant cross section as a function of p_T for $\pi^\pm$ production at 90° obtained in this way are shown in figs. 21 and 22. Shown also are the ISR data obtained by the Saclay-Strasbourg Collaboration [12] at c.m. energies equivalent to incident laboratory momenta between 500 and 1500 GeV/c (the data at different energies are identical within errors) and $0.2 < p_T < 1.2$ GeV/c at 90°, and by the British-Scandinavian Colla-

boration [13] at an equivalent laboratory momentum of 1500 GeV/c (data at lower energies are again identical within errors), $0.13 < p_T < 1.0$ GeV/c, $\theta^* = 89°$.

In the region $0.3 < p_T < 1.0$ GeV/c the 12 and 24 GeV/c pion spectra can be well fitted by an exponential in p_T,

$$E\frac{d^3\sigma}{dp} = A \exp(-Bp_T). \tag{12}$$

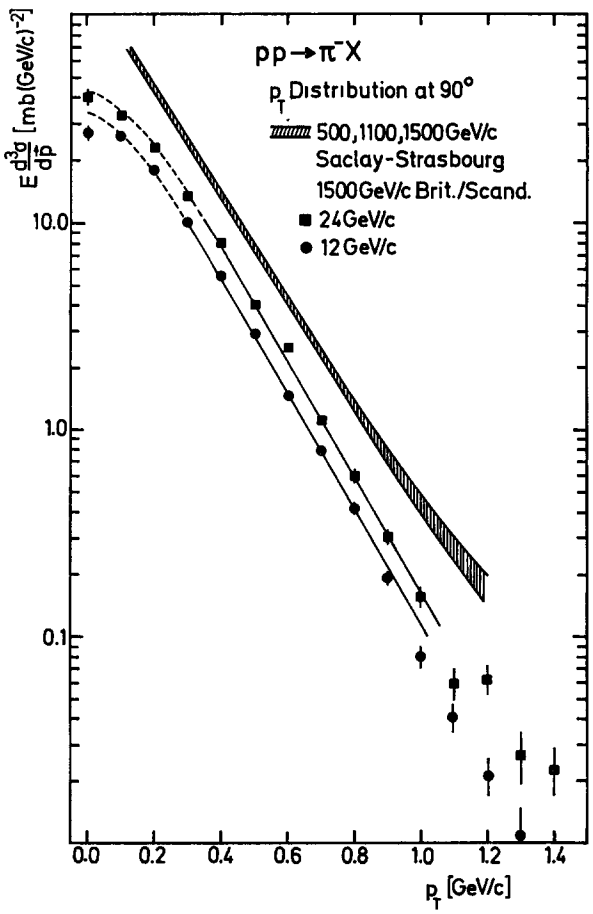

Fig. 22. Invariant cross section at 90° in the c.m. system for π^- as a function of p_T. The solid straight line is an exponential fit in p_T, the dashed curve is an exponential fit in the generalized longitudinal mass μ.

The fits are shown as solid straight lines in figs. 21 and 22 together with corresponding fits to the ISR data. The values of A and B are listed in table 5. Comparison of the 12 and 24 GeV/c data with the ISR data suggests that the p_T behaviour of the invariant cross section is exponential with nearly the same slope parameter B from 12 GeV/c

Table 5a

Values of parameters A, B and C from a fit to the distribution at 90° with $A \exp(-Bp_T)$ and $A' \exp(-C\mu)$, respectively. A (mb (GeV/c)$^{-2}$), B (GeV/c)$^{-1}$, C (GeV^{-1}), $\mu = \sqrt{m^2 + \beta_0^2 p_T^2}$

		12 GeV/c	24 GeV/c	1500 GeV/c
π^-	A	73.8 ±2.3	93.4 ±3.3	155 ±5
	B	6.55 ±0.07	6.28 ±0.07	6.06 ±0.10
	C	7.26 ±0.05	6.61 ±0.05	
π^+	A	115.4 ±3.5	136.4 ±4.9	180 ±10
	B	6.25 ±0.07	6.14 ±0.07	6.22 ± 0.10
	C	7.11 ±0.05	6.48 ±0.05	
P	A	32.4 ±2.8	15.7 ±2.7	11.6 ±1.2
	B	4.46 ±0.10	4.06 ±0.18	4.16 ±0.13
	C	7.43 ±0.13	6.07 ±0.2	

Table 5b

Values of parameter D from a fit with $A'' \exp(-D\mu)$ to the distributions for various intervals of the cms rapidity $|y^*|$. D (GeV^{-1}), $\mu = \sqrt{m^2 + \beta_0^2 p_T^2}$

	12 GeV/c		24 GeV/c	
	$0 \leq \|y^*\| < 0.4$	$0.4 \leq \|y^*\| < 0.8$	$0 \leq \|y^*\| < 0.4$	$0.4 \leq \|y^*\| < 0.8$
π^-	7.25 ±0.25	7.60 ±0.15	6.50 ±0.10	6.75 ±0.15
π^+	7.35 ±0.20	7.15 ±0.15	7.05 ±0.10	6.75 ±0.30
K_s^0	8.25 ±0.40	9.25 ±0.50	6.90 ±0.25	7.55 ±0.30
p	7.50 ±0.10	8.20 ±0.15	6.35 ±0.15	7.00 ±0.10
Λ	10.00 ±0.30	11.60 ±0.35	9.90 ±0.60	9.35 ±0.50

to 1500 GeV/c, indicating a very early limiting behaviour of the shape of the p_T distribution.

Below $p_T = 0.2$ GeV/c the distributions flatten toward $p_T = 0$, both at 12 and 24 GeV/c. The behaviour of the cross section in the low p_T region at ISR energies, where the data extend down to $p_T \approx 0.2$ GeV/c, is hardly compatible with the behaviour at 24 GeV/c, while the possibility of a continuing exponential behaviour cannot be excluded.

For the reaction

$$pp \to p + X$$

at 90°, we see from fig. 23 that the proton spectra can also be fitted by exponentials in p_T, but with a slope less steep than for pions, and with a flattening-off already at

larger p_T. We will discuss in the next section an attempt at a unified parametrization of the p and $\pi^{\pm}$ spectra for all p_T in terms of an exponential dependence on longitudinal mass. But since the available ISR data here (Saclay-Strasbourg Collaboration, equivalent lab. momentum 1500 GeV/c) do not extend below the p_T region where the data can be approximated by eq. (12), we may as well study here the s dependence of the spectrum shape in terms of the fitted slope parameter B. With the fitted A and B (for $p_T \geq 0.6$ GeV/c) at each energy given in table 5, the fits to eq. (12) are shown as solid

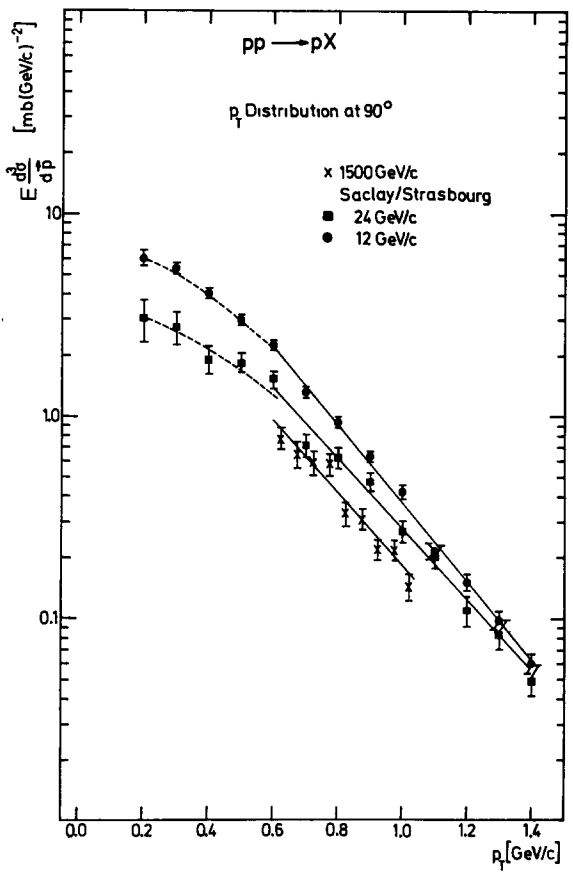

Fig. 23. Invariant cross section at 90° in the c.m. system for p as a function of p_T. The solid straight line is an exponential fit in p_T, the dashed curve is an exponential fit in the generalized longitudinal mass μ.

straight lines in fig. 23. As was the case for the pion spectra the slope parameter B is essentially the same at 24 and 1500 GeV/c while the 12 GeV/c slope appears to be somewhat steeper.

In table 6 we give the cross sections at 90° integrated over p_T, $d\sigma/dy^*$ at $y^* = 0$, for inclusive production of $\pi^{\pm}$ and p at 12 and 24 GeV/c, as obtained from the full

Table 6
Cross sections $d\sigma/dy^*$ in mb at $y^* = 0$ at 12 and 24 GeV/c

	12 GeV/c	24 GeV/c
π^-	9.52 ±0.08	13.25 ±0.12
π^+	17.12 ±0.13	20.04 ±0.20
p	7.34 ±0.13	4.31 ±0.18

p_T distributions. For the ISR pion data we can only estimate $d\sigma/dy^*$ since the data do not extend down to $p_T = 0$. We estimate upper and lower limits, respectively, by assuming either an exponential behaviour for all p_T, or a distribution flattening off at $p_T = 0$ in a similar manner as observed at 24 GeV/c. These estimates are plotted in fig. 24 together with our 12 and 24 GeV/c data against $p_{lab}^{-\pm}$. This dependence is suggested by the Mueller-Regge analysis [14]. For the proton cross section at ISR energies we assumed the same p_T dependence as at 24 GeV/c, with a 20% error. For $\pi^\pm$ other data [15] available below 300 GeV/c are included in fig. 24.

The following conclusions can be drawn from figs. 21-24 about the s dependence at 90°. The energy dependence is less for π^+ than for π^-. Indeed the π^+ cross sections shown in fig. 21 at 24 GeV/c and at ISR energies are not very different in the

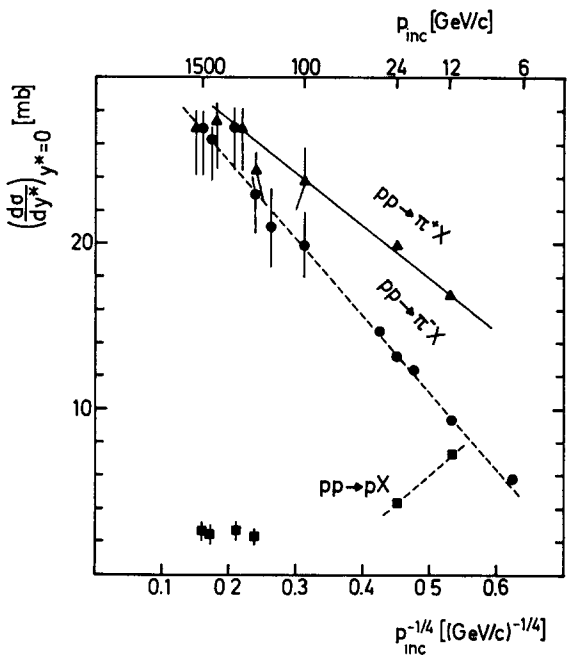

Fig. 24. Integrated invariant cross section at 90° for $\pi^\pm$ and p as a function of $p_{inc}^{-\pm}$.

region $p_T > 0.2$ GeV/c where data at both energies exist. Therefore if $d\sigma/dy^*$ for π^+ increases from 24 GeV/c to ISR energies, it must come mainly from an increase in the small p_T region. The increase of the cross section for π^- is larger, it is 40% between 12 and 24 GeV/c, and about 60% between 24 GeV/c and ISR energy. A linear dependence of the pion cross sections on $p_{lab}^{-\frac{1}{2}}$ up to ISR energies is not excluded [16, 17].

At lower energies a large fraction of the particles observed in the central region is expected to come from the (target and projectile) proton fragmentation; this fraction presumably decreases, at 90° in the c.m. system, when one goes from 12 GeV/c to 24 GeV/c. The strong decrease observed of the proton cross section (fig. 24) is probably a result of this effect. The fact that the π^+ cross section is larger than the π^- cross section at 24 GeV/c, while they agree at ISR energies, may also be due (at least partly) to proton fragmentation favouring π^+ over π^-.

7. Dependence on longitudinal mass

We return to the question of attempting a unified description of the transverse-momentum spectra in the central region for all p_T. As plotted in figs. 21-23, the π and p spectra are quite dissimilar in appearence. It has been suggested [18] that the cross section may be a universal exponential function of the longitudinal mass $m_L = \sqrt{m^2 + p_T^2}$ or its covariant generalization [19] $\mu = \sqrt{m^2 + n^2}$, where for a reaction $A + B \to C + X$,

$$n_\alpha = \frac{2\varepsilon_{\alpha\beta\gamma\delta} P_A^\beta P_B^\gamma P_C^\delta}{(P_A + P_B)^2}, \tag{13}$$

$$n^2 = -n_\alpha n^\alpha. \tag{14}$$

In our case, n^2 reduces to $\beta_0^2 p_T^2$, where β_0^2 is the incoming c.m. velocity squared of either proton, giving

$$\mu = \sqrt{m^2 + \beta_0^2 p_T^2} \underset{s \to \infty}{\to} m_L.$$

In fig. 25 we plot logarithmically $E\, d^3\sigma/dp$ for pions and protons against a single continuous μ scale for various ranges of the cms rapidity $|y^*|$, with superposed fitted straight lines

$$E \frac{d^3\sigma}{dp} \equiv \frac{1}{\pi} \frac{d^2\sigma}{dy^* dp_T^2} = A' \exp(-C\mu). \tag{15}$$

For the more central y^* interval ($|y^*| < 0.4$, fig. 25a), the fits are seen to be surprisingly good over all p_T, with very similar slope parameters C (see table 5a for fitted

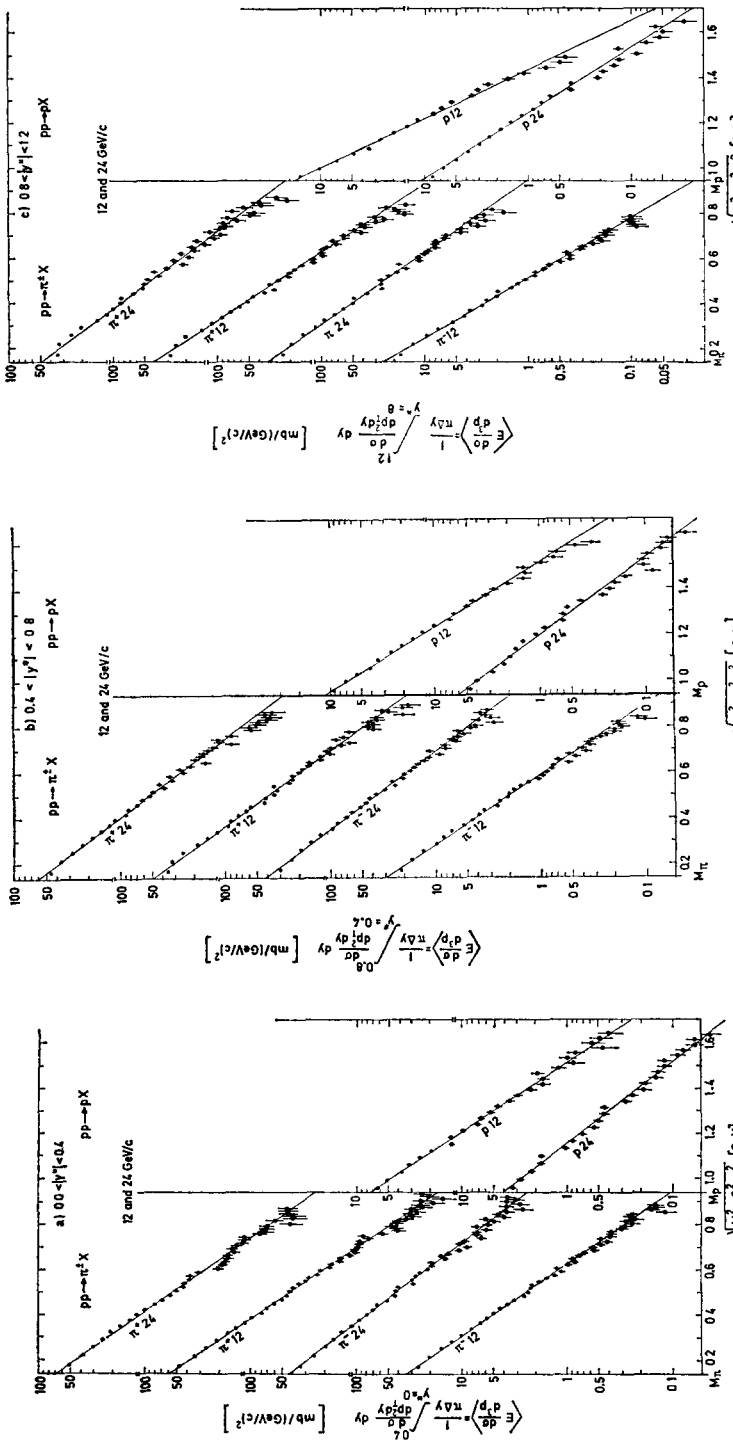

Fig. 25. Invariant cross section as a function of the generalized longitudinal mass μ for $\pi^{\pm}$ and p in different y^* regions. Superposed lines are best fits to exponentials in μ.

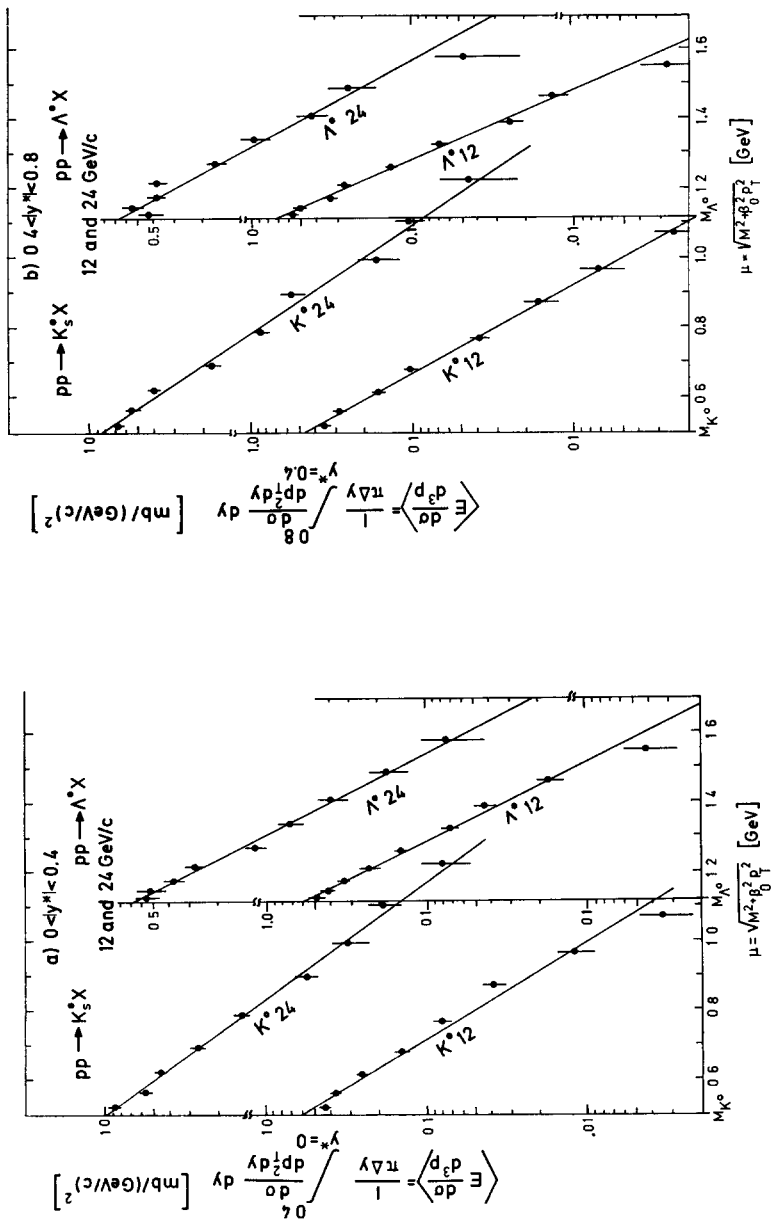

Fig. 26. Invariant cross section as a function of the generalized longitudinal mass μ for K^0_s and Λ in different y^* regions. Superposed lines are best fits to exponentials in μ.

parameters at $y^* = 0$) for all particle species. However, the tendency of the pion data to flatten out relative to $\exp(-C\mu)$ at small p_T, which is clearly evident in the interval $0.4 < |y^*| < 0.8$ (and gets more pronounced as one goes further out into the fragmentation region, see fig. 25b and c), is already somewhat in evidence below $|y^*| = 0.4$. The fit of eq. (15) to our 90° data is shown in figs. 21-23 by the dashed curves (displayed only in the p_T region below the fits to eq. (12)). The departure of the proton spectra from an exponential in p_T is seen to be very well described, but the tendency of the pion spectra to fall somewhat away from the exponential in μ at low p_T seems to persist down to $y^* = 0$ (the points at $p_T = 0$, being extrapolated, are not included in the fits).

The use of the covariant μ rather than the simple longitudinal mass $\sqrt{m^2+p_T^2}$ gives in general a modest improvement in the χ^2's for the pion fits at small p_T (at the cost of a greater energy dependence for the slope parameter), but one cannot make a significant distinction between these alternatives here. Neither seems to provide a complete description of the low p_T pion data, at least at our energy. For the heavier proton, the μ and m_L fits are equally good.

For K_s^0 and Λ the invariant cross sections as a function of μ are also, within the experimental uncertainties, described well by exponentials. This is shown in figs. 26a, b. Table 5b gives the fitted slope parameters corresponding to the straight lines shown for the various y^* intervals in figs. 25 and 26.

8. Factorization in the proton fragmentation region

Finally we investigate whether the single-particle distributions in the target proton fragmentation region are independent of the quantum numbers of the projectile or, equivalently, whether the (presumably pomeron-dominated) exchange factorizes. We therefore compare in fig. 27 our $\pi^\pm$ spectra from 12 and 24 GeV/c pp interactions with the published spectra from π^+p, π^-p, K^+p and γp interactions at comparable incident momenta [20-24]. For the comparison we scaled our pp data, which are shown as curves, by the ratio of the pomeron couplings to the beam particle, i.e. with $\sigma_T^\infty(K^+p)/\sigma_T^\infty(pp) \approx 0.466$, $\sigma_T^\infty(\pi^\pm p)/\sigma_T^\infty(pp) \approx 0.615$, and $\sigma_T^\infty(\gamma p)/\sigma_T^\infty(pp) = 0.00264$, respectively. The plotted invariant cross sections $d^3\sigma/(d\boldsymbol{p}/E)$ are integrated over p_T^2. The abscissa variables had to be chosen in accord with the published plots from the other experiments; therefore we use here the longitudinal variables y^{lab}, $p_\parallel^{lab}$ and x.

In figs. 27a, b, c the reactions compared with our data are, in the sense of Chan et al. [24], exotic as are our $\pi^\pm$ inclusive reactions. In these cases the overall agreement in the proton fragmentation region is seen to be reasonably good. An exception are the two points in fig. 27c at small p_T and large $|x|$ from the 11.8 GeV/c $K^+p \to \pi^-X$ experiment [20] which, if true, indicate a very strong deviation from factorization. We remark however that this discrepancy occurs in a region of quite small cross sections, so that even a small experimental bias or background may have a relatively large effect. One should also point out that for $p_T < 0.2$ GeV/c the $K^+p \to \pi^-X$ data

[20] (fig. 27c) show distinctly less convexity than the $pp \to \pi^- X$ data. This is perhaps a departure from factorization. On the other hand, the less convincing comparison in fig. 27b [22] should be viewed in conjunction with fig. 27a [21] where good agreement is seen with the same reaction.

Figures 27d, e, f show the comparison of some non-exotic reactions with our scaled pp data. The $\pi^- p \to \pi^- X$ data at 18.5 GeV/c [21] (fig. 27d) are still quite far above

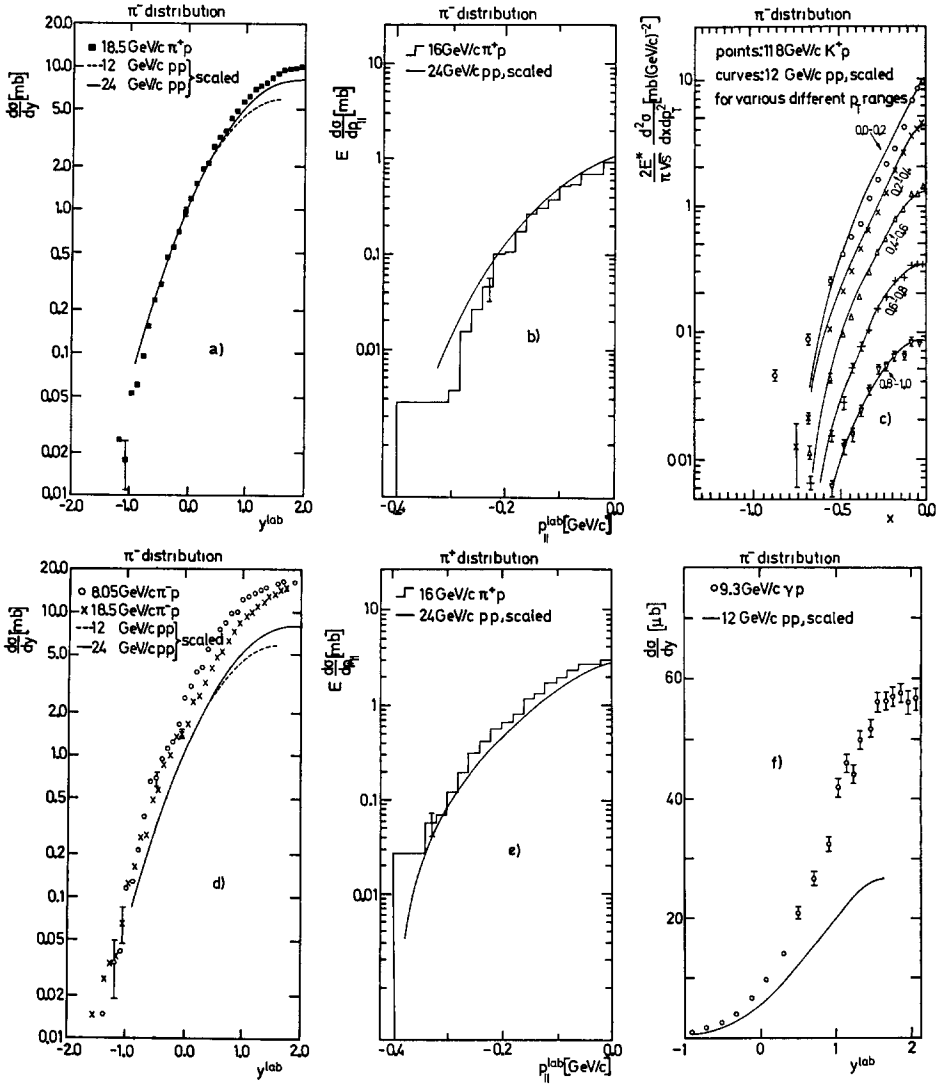

Fig. 27. Comparison of $\pi^\pm$ distributions from various other experiments using $\pi^\pm$, K^+ or γ beams with our data (p beam). The p beam cross sections, multiplied by the ratios $\sigma^\infty_{\pi p}/\sigma^\infty_{pp}$, $\sigma^\infty_{Kp}/\sigma^\infty_{pp}$ or $\sigma^\infty_{\gamma p}/\sigma^\infty_{pp}$ respectively, are shown as curves.

our $pp \to \pi^- X$ distribution; in fact Shephard et al. [21] point out that their non-exotic data (fig. 27d) tend towards their exotic spectrum (fig. 27a), and hence towards our scaled $pp \to \pi^- X$ spectrum (see fig. 27a), like $s^{-\frac{1}{2}}$ in the proton fragmentation region. It is also clear that at these energies the target proton fragments are still not well sep-

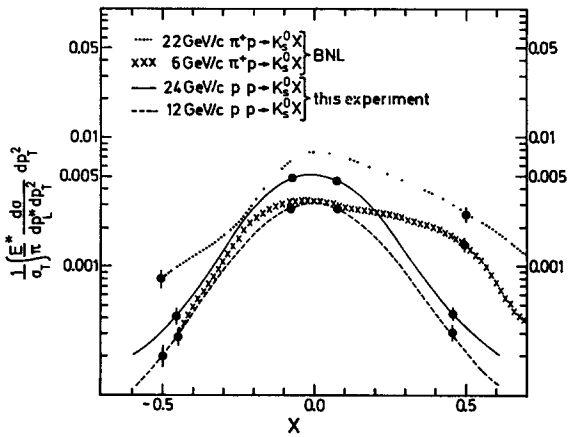

Fig. 28. Comparison of the invariant cross sections *versus* x for K^0_s from $\pi^+ p$ with our pp data. The cross sections, divided by the asymptotic total cross sections, are shown as curves; some representative points are shown with error bars.

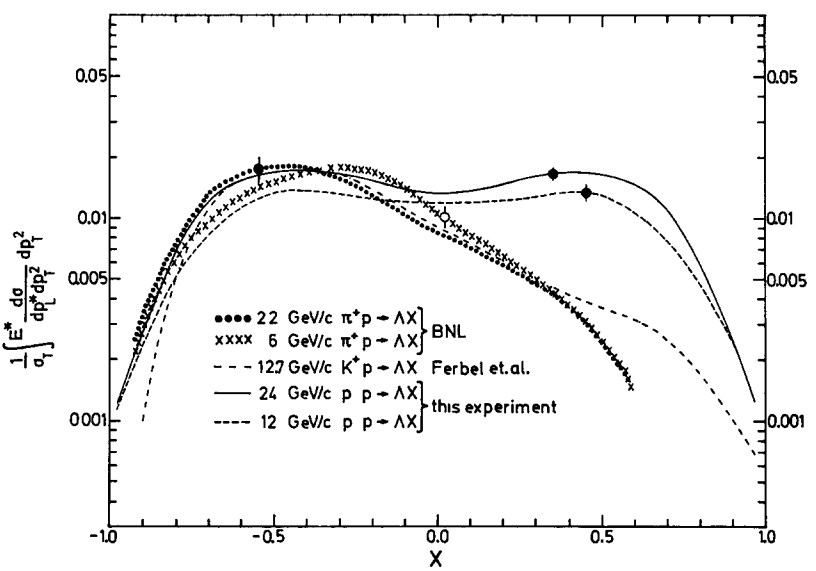

Fig. 29. Comparison of the invariant cross sections *versus* x for Λ from $\pi^+ p$ and $K^+ p$ with our pp data. The cross sections, divided by the asymptotic total cross sections, are shown as curves, some representative points are shown with error bars.

arated kinematically from the projectile fragments and pionization products. To a lesser degree, also the non-exotic $\pi^+ p \to \pi^+ X$ spectrum at 16 GeV/c [22] (fig. 27e) is found to lie above our $pp \to \pi^+ X$ data. The same is true for the comparison of our π^- data with the non-exotic $\gamma p \to \pi^- X$ data [23] (fig. 27f); these latter data have an energy dependence compatible with a drop like $s^{-\frac{1}{2}}$ and may assume the same limiting behaviour as the $pp \to \pi^- X$ data.

Finally figs. 28 and 29 show a comparison of our $pp \to K_s^0 X$ and $pp \to \Lambda X$ inclusive x distributions, with corresponding distributions obtained with incident π^+ and K^+ beams of similar momenta [25, 26]. In the beam fragmentation regions ($x > 0$) these spectra show very large differences; in the proton target fragmentation region, on the other hand, the dependence on the beam quantum numbers is much smaller although still significant. Note that all the reactions compared in figs. 28 and 29 are exotic.

9. Summary

From the cross sections, multiplicity data and the various single particle inclusive spectra presented, the following main points can be abstracted:

(i) The $\pi^\pm$ double-differential spectra show only some 10% to 20% change between 12 GeV/c and 1500 GeV/c incident momentum in the proton fragmentation region, and a similarly small change between 24 GeV/c and 1500 GeV/c in the central region, when compared at fixed y^{lab} and p_T.

(ii) The K_s^0 yield increases by a factor of about 2 between 12 and 24 GeV/c, and by another factor of 2 between 24 GeV/c and 205 GeV/c; however at $p_T \approx 0$ in the proton fragmentation region it may be less energy-dependent (at fixed y^{lab}).

(iii) The kaon to pion ratio is $\sim \frac{1}{30}$ in the central region but only $\sim \frac{1}{100}$ in the proton fragmentation region (at 24 GeV/c); this may be connected with the fact that the K_s^0 have higher average $\langle p_T \rangle$ than the pions.

(iv) The invariant proton spectrum decreases in the central region with increasing p_{inc}, while the Λ, $\Sigma^\pm$ and $\bar{\Lambda}$ spectra increase. Like the p, also the Λ spectrum is seen to develop a dip in the center of the y^* distribution.

(v) The $\pi^\pm$ and p transverse momentum spectra at 90 deg in the cms ($x = y^* = 0$) show a flattening near $p_T = 0$ when plotted logarithmically against p_T. In the region where the behaviour is exponential, the slope parameter is the same at 24 GeV/c and at 1500 GeV/c.

(vi) When plotted *versus* the generalized longitudinal mass μ, the transverse distributions are nearly exponential, with slopes that become generally smaller with increasing incident energy.

(vii) A behaviour of the "plateau height" $(d\sigma/dy)_{y^*=0}$ for pions of the form $A+Bp_{inc}^{-\frac{1}{2}}$, as suggested by the Mueller-Regge approach, is compatible with the data between $p_{inc} = 12$ GeV/c and ISR energies.

(viii) The longitudinal pion spectra in the proton target fragmentation region factorize with respect to the beam particle, if the quantum numbers of the corresponding Mueller diagram are exotic. Corresponding spectra for non-exotic reactions seem to approach the exotic ones from above.

(ix) At 12 and 24 GeV/c there is only a weak correlation between the mean number of π^0's produced and the number of charged secondaries in an event, while at higher energies a strong positive correlation has been observed.

We are indebted to the CERN operation crews of the PS and of the 2m bubble chamber for their excellent cooperation. We wish to particularly thank H.H. Nagel and J. Seyerlein, who have been responsible for the development of our Flying-Spot Digitizers. Finally we thank A. Brandt, E. Lohrmann, H.H. Nagel and M.W. Teucher for advice, help, criticism, and active support. This work was supported by the Bundesministerium für Forschung und Technologie.

References

[1] J.V. Allaby et al., Proc. of the 4th Int. Conf. on high energy collisions, Oxford, vol. II (1972) p. 85.
[2] H.J. Mück et al., Phys. Letters 39B (1972) 303;
H.J. Mück et al., Proc. of the 4th Int. Conf. on high energy collisions, Oxford, vol. II (1972) p. 117;
H.J. Mück et al., Proc. of the 4th Int. Conf. on high energy collisions, Oxford, vol. II (1972) p. 127†;
U. Idschok et al., Contribution to the 16th Int. Conference on high energy physics, NAL, Batavia, 1972;
U. Idschok et al., Report MPI-PAE/Exp. El. 29 (1973), to be published in Nucl. Phys. B.
[3] Particle Data Group, UCRL-20000 NN (1970).
[4] C.G. Beznogigk et al., Phys. Letters 43B (1973) 85.
[5] T.M. Knasel, Report DESY 70/3 (1970).
[6] H. Fesefeldt, Thesis, University of Hamburg (1973); Internal report DESY F1-73/11, unpublished.
[7] J.H. Campbell et al., ANL/HEP 7311 (1973);
G. Charlton et al., Phys. Rev. Letters 29 (1972) 1759.
[8] G. Neuhofer et al., quoted by M. Jacob in Proc. of the Int. Conf. on high energy physics, Chicago-Batavia (1972), vol. 3, p. 373.
[9] J.C. Sens, Proc. of the 4th Int. Conf. on high energy collisions, Oxford, vol. I (1972) p. 177;
A. Bertin et al., Phys. Letters 38B (1972) 260;
L.G. Ratner et al., Phys. Rev. Letters 27 (1971) 68;
Saclay-Strasbourg Collaboration, quoted by Sens loc. cit.

† In the Proc. fig. 2 on page 131 should be replaced by fig. 2 of page 122, while the correct fig. 2 for page 122 is given by in the Phys. Letters article, cited above; the figure captions should not be changed.

[10] G. Charlton et al., Phys. Rev. Letters 30 (1973) 574.
[11] W.M. Dunwoodi et al., quoted by B.Y. Oh et al., Nucl. Phys. B49 (1972) 13.
[12] Saclay-Strasbourg Collaboration, quoted by Sens [9]; Phys. Letters 41B (1972) 547.
[13] British-Scandinavian Collaboration, Contribution to the 4th Int. Conf. on high energy collisions, Oxford, (1972); Phys. Letters 47B (1973) 75.
[14] A.H. Muller, Phys. Rev. D2 (1970) 2963.
[15] W.H. Sims et al., Nucl. Phys. B41 (1972) 317;
E. Gellert, Report LBL-784 (1972);
C. Bromberg et al., Report UR-460 (1973);
Y. Cho et al., Report ANL/HEP 7316 (1973).
[16] T. Ferbel, Phys. Rev. Letters 29 (1972) 448; Phys. Rev. D8 (1973) 2321.
[17] H. Meyer and W. Struczinski, Report DESY 72/40 (1972).
[18] S. Barshay and Y.A. Chao, Phys. Letters 38B (1972) 225.
[19] E. Leader and M.R. Pennington, Phys. Rev. Letters 27 (1971) 1325.
[20] W. Ko and R.L. Lander, Phys. Rev. Letters 26 (1971) 1064.
[21] W.D. Shephard et al., Phys. Rev. Letters 27 (1971) 1164; 28 (1972) 260(E).
[22] J.V. Beaupre et al., Phys. Letters 37 (1971) 432.
[23] K.C. Moffeit et al., Phys. Rev. D5 (1972) 1603.
[24] Chan Hong-Mo et al., Phys. Rev. Letters 26 (1971) 672.
[25] D.J. Crennell et al., Phys. Rev. Letters 28 (1972) 643.
[26] S. Stone et al., Phys. Rev. D5 (1972) 1621.